Materials Science & Engineering C 124 (2021) 112089

Contents lists available at ScienceDirect

Materials Science & Engineering C

journal homepage: www.elsevier.com/locate/msec

Chitosan and chitosan/PEG nanoparticles loaded with indole-3-carbinol: Characterization, computational study and potential effect on human bladder cancer cells

Micael Nunes Melo [a,b], Fernanda Menezes Pereira [a,b], Matheus Alves Rocha [a,b], Jesica Gonçalves Ribeiro [a,b], Alexander Junges [c], Wesley Formentin Monteiro [d], Fernando Mendonça Diz [e], Rosane Angélica Ligabue [e], Fernanda Bueno Morrone [f], Patrícia Severino [a,b], Alini Tinoco Fricks [a,b,*]

[a] Tiradentes University - UNIT, Av. Murilo Dantas 300, 49032-490 Aracaju, SE, Brazil
[b] Institute of Technology and Research - ITP, Av. Murilo Dantas 300, 49032-490 Aracaju, SE, Brazil
[c] Department of Food Engineering, URI - Erechim Av. Sete de Setembro, 1621, 99709-910 Erechim, Rio Grande do Sul, Brazil
[d] Chemistry Institute, Federal University of Rio Grande do Sul - UFRGS, Av. Bento Gonçalves 9500, 91501-970 Porto Alegre, RS, Brazil
[e] School of Technology, Pontifical Catholic University of Rio Grande do Sul - PUCRS, Av. Ipiranga 6681, 90619-900 Porto Alegre, RS, Brazil
[f] School of Life and Health Sciences, Pontifical Catholic University of Rio Grande do Sul - PUCRS, Av. Ipiranga 6681, 90619-900 Porto Alegre, RS, Brazil

ARTICLE INFO

Keywords:
Bladder cancer
Chitosan
Indole-3-carbinol
Nanoparticle
Polyethylene glycol

ABSTRACT

Indole-3-carbinol (I3C) is a plant molecule known to be active against several types of cancer, but some chemical characteristics limit its clinical applications. In order to overcome these limitations, polymeric nanoparticles can be used as carrier systems for targeted delivery of I3C. In this study, chitosan and chitosan/polyethylene glycol nanoparticles (CS NP and CS/PEG NP, respectively) were prepared to encapsulate I3C by ionic gelation method. The polymeric nanoparticles were characterized by Dynamic Scattering Light (DLS), Zeta Potential (ZP), Fourier Transform Infrared (FTIR) spetroscopy, X-Ray Diffraction (XRD), Thermogravimetric Analysis (TGA), Differential Scanning Calorimetry (DSC), and Field Emission Gun Scanning Electron Microscopy (FEG-SEM). I3C release testing was performed at an acidic media and the interactions between I3C and chitosan or PEG were evaluated by Density Functional Theory (DFT). Cytotoxicity of nanoparticles in bladder cancer T24 cell line was evaluated by the Methyl-thiazolyl-tetrazolium (MTT) colorimetric assay. The average size of the nanoparticles was observed to be in the range from 133.3 ± 3.7 nm to 180.4 ± 2.7 nm with a relatively homogeneous distribution. Samples had relatively high positive zeta potential values (between +20.3 ± 0.5 mV and + 24.3 ± 0.5 mV). Similar encapsulation efficiencies (about 80%) for both nanoparticles were obtained. Physicochemical and thermal characterizations pointed to the encapsulation of I3c. *electron* microscopy showed spherical particles with smooth or ragged surface characteristics, depending on the presence of PEG. The mathematical fitting of the release profile demonstrated that I3C-CS NP followed the Higuchi model whereas I3C-CS/PEG NP the Korsmeyer-Peppas model. Chemical differences between the nanoparticles as based on the I3C/CS or I3C/PEG interactions were demonstrate by computational characterization. The assessment of cell viability by the MTT test showed that the presence of both free I3C and I3C-loaded nanoparticles lead to statistically significant reduction in T24 cells viability in the concentrations from 500 to 2000 μM, when comparison to the control group after 24 h of exposure. Thus, CS and CS/PEG nanoparticles present as feasible I3C carrier systems for cancer therapy.

1. Introduction

Bladder cancer is the 10th most frequently-diagnosed cancer all over the world and the ninth leading cause of cancer death in men [1], especially because a considerable proportion of patients with bladder cancer are initially diagnosed with advanced stages of the disease [2]. For this reason, radical cystectomy combined with neoadjuvant/adjuvant chemotherapy is the standard treatment. However, this approach

* Corresponding author at: Tiradentes University - UNIT, Av. Murilo Dantas 300, 49032-490 Aracaju, SE, Brazil.
E-mail address: alinitf@yahoo.com.br (A.T. Fricks).

https://doi.org/10.1016/j.msec.2021.112089
Received 20 January 2021; Received in revised form 11 March 2021; Accepted 26 March 2021
Available online 31 March 2021

has a high rate of acute and chronic complications, being particularly critical for submitted patients, since they are generally older and have multiple comorbidities [3]. On this regard, the search for highly efficient and less harmful alternatives for the treatment of advanced stages of this disease is necessary.

Over the past two decades, many studies have demonstrated the action of indole compounds as potentially effective agents against bladder cancer, such as indole-3-acetic acid [4], Go-6976 [5], apaziquone [6], 5-hydroxyindole-3-acetic acid [7], arylindolylpropenones [8], and 3,3′-diindolylmethane [9]. In this context, indole-3-carbinol (I3C) is an indole compound produced endogenously from natural glycosinolates contained in a wide variety of plant food substances, including members of the Cruciferae family, and particularly members of the genus *Brassica*, such as broccoli, cabbage, cauliflower, brussels sprouts, china cabbage, radish, turnip and rapeseed [10], being one of the metabolites resulting from the enzymatic oxidation of indole-3-acetic acid [11], as well as to be the precursor of 3,3′-diindolylmethane [12].

It is known that I3C exerts anti-cancer effects mediated by cell cycle regulation, induction of apoptosis, transcription, cell signal transduction, hormonal homeostasis, inhibition of angiogenesis, suppression of cell invasion, DNA repair, and anti-inflammatory activity [13,14]. The anti-cancer properties of I3C has been detected in several target organs, including breast [15], prostate [16], cervix [17], skin [18], lung [19], blood [20], liver [21], and colon [22]. Although the wide variety of tumor cell lines studied, the anti-tumor effect of I3C has not been evaluated for bladder cancer until the present moment as far as we know.

Despite I3C presents therapeutic activity against several types of tumors, it also has some limitations: (a) low water solubility, which limits its administration; (b) rapid oxidation, metabolization, and elimination, which decreases its serum level and bioavailability [23]; (c) photosensitivity; and (d) thermosensitivity [24]. These disadvantages are responsible for limiting the clinical applications of this compound. In order to overcome these limitations, some studies have reported the incorporation of I3C in nanostructured systems for cancer therapy [25–27].

Progress in the field of nanomedicines in cancer treatment has shown the use of polymer-based nanoparticles as material for the efficient delivery of several anticancer drugs in recent decades [28]. Currently, there are several polymeric nanoparticles that have not been clinically approved and are currently undergoing clinical trials [29]. Among polymeric nanocarriers used to treat cancer, polymeric nanoparticles based on chitosan are presented as an alternative for encapsulation of I3C, since chitosan is one of the most promising biopolymer in the development of nanoparticles [30–32]. The reasons for using chitosan nanoparticles in cancer treatment are their physicochemical and biological properties [33]. Chitosan is a linear cationic aminopolysaccharide derived from chitin, a polymer obtained mainly from crustacean shells. It has low toxicity, is biodegradable, biocompatible, non-antigenic, hydrophilic, and biofunctional [34]. The flexibility of the chitosan chain and the possibility to forming hydrogen bonds with carboxylic and hydroxyl groups are factors that attribute great applicability to this polymer [35]. Thus, chitosan may interact electrostatically with polyanionic molecules to form nanoparticles from low complexity processes, such as ionotropic gelation, resulting in particles less than 200 nm [36].

Due to their small diameter, chitosan nanoparticles are able to penetrate tumor tissue through gaps in the vascular endothelium of tumor tissue and accumulate with a high concentration in this region for a long time due to insufficient venous and lymphatic clearance, through the enhanced permeability and retention (EPR) effect [37]. In addition, the positive chitosan charge favors a mechanism of cell uptake, since it interacts with the negatively charged cell membrane, promoting a structural disorder and increasing the fluidity of the membrane, providing cellular absorption [38]. Moreover, chitosan-based materials are sensitive to exposure in slightly acidic media, such as the tumor microenvironment [39] and the interior of endolysosomal organelles [40], favoring the release of active molecules both in the tumor microenvironment and in the cell interior. Furthermore, the use of polyethylene glycol in the composition of chitosan nanoparticles can be explored due to the ability of this hydrophilic polymer to prolong the circulation time of the nanocarriers in the bloodstream and increasing the tumor exposure to the encapsulated drug [41].

Recently, some studies have shown some characteristics of pharmaceutical interest, as well as the efficiency of nanoparticulate systems involving chitosan nanocapsules coated with polyethylene glycol (PEG). This axis proved to be able to improve the drug delivery system, as well as to improve the stability, biodistribution, internalization of drugs with antitumor properties. For example, Hefnawy *et al* (2020) successfully development and evaluation of a novel dual-ligand functionalized core-shell chitosan-based nanocarrier for the selective delivery of doxorubicin for treatment of hepatocellular carcinoma with enhance the intracellular uptake (*in vitro* study), as well as enhanced safety profile compared to the conventional doxorubicin (*in vivo* study) [42]. Caban-Toktas *et al* (2020) reported an approach with positively-charged chitosan-modified PEG nanoparticles loaded R-flurbiprofen and paclitaxel exhibited higher therapeutic activity to suppress glioblastoma growth in study with animal model [43]. Besides, Zhang et al. (2019) prepared and assessed *in vitro* and *in vivo* galactosylated chitosan nanoparticles loaded with triptolide (GC-TP-NP). This study showed GC-TP-NPs cellular uptake was greater than free TP *in vitro* and accumulated preferentially in the liver tumor tissue *in vivo* [44].

In this context, this work proposes the development of chitosan nanoparticles and associated chitosan/PEG nanoparticles for I3C encapsulation. Also, computational studies to estimate the interactions between I3C and chitosan or PEG were performed. In addition, *in vitro* cytotoxic effect of free I3C and I3C-loaded nanoparticles in an invasive human bladder carcinoma cell line was evaluated (T24).

2. Materials and methods

2.1. Materials

Indole-3-carbinol (C_9H_9NO, ≥96% purity, CAS Number 700–06-1), Chitosan (Medium Molecular Weight, 190–310 kDa, CAS Number 9012-76-4), Sodium Tripolyphosphate ($Na_5P_3O_{10}$, 85%, CAS Number 7758-29-4) and Polyethylene glycol (Mw = 8000 Da, CAS Number 25322–68-3) were purchased from Sigma-Aldrich Co. (St. Louis, USA). Acetic acid ($C_2H_4O_2$, CAS Number 64–19-7), Sodium hydroxide (NaOH, CAS Number 1310-73-2) and other reagents were obtained from Vetec Ltd. (Rio de Janeiro, Brazil). For biological assays, the reagents used were RPMI-1640 (Catalog Number 11–875-093), fetal bovine serum (FBS, Catalog Number 26–140-079), penicillin-streptomycin 10,000 U/mL (Catalog Number 15–140-148), amphotericin B (Fungizone®, Catalog Number 15–290-018), and 0.5% trypsin/EDTA solution (Catalog Number 15–400-054), obtained from Gibco Laboratories (Carlsbad, USA). MTT (3-(4,5-dimethylthiazol-2-yl)-2,5-diphenyltetrazolium bromide, CAS Number 298–93-1) solution at 5 mg/mL in PBS and 90% culture medium supplemented with 10% FBS (CAS Number 9014-81-7) were sourced from Sigma-Aldrich (Ontario, Canada). All other chemicals and solvents were analytical grade, and solutions were prepared using ultrapure or distilled water.

2.2. Methods

2.2.1. Preparation of I3C standard solution and calibration curve

The I3C stock solution (3.5 mM) was prepared in pure ethanol and diluted in a range from 4.5 to 290 μM. The standard calibration curve for I3C was obtained by the absorbance measurement of the diluted solutions in a Libra S22 UV/Vis Spectrophotometer (Biochrom – Cambridge, UK) at a wavelength of 280 nm [45].

2.2.2. Preparation of free and I3C-loaded CS nanoparticles and CS/PEG nanoparticles

Chitosan nanoparticles (CS NP) were prepared by the ionic gelation method as described previously with modifications [46]. Chitosan (1.0 mg/mL) was dispersed in acetic acid aqueous solution 0.175% (*v*/v) and magnetically stirred (C-MAG HS 7, IKA – Staufen, Germany) at 100 rpm and heated to 50 °C for 2 h. The obtained dispersion was filtered under vacuum through a 0.45 mm pore size cellulose acetate membrane and the pH (D-22, Digimed - São Paulo, Brazil) was adjusted to 5.0 using sodium hydroxide (0.5 M). Tripolyphosphate (1.0 mg/mL) was dissolved in water by manual stirring. CS Nanoparticles were produced after the dropwise addition of TPP solution (28 mL) in the aqueous chitosan dispersion (70 mL). The resulting opalescent suspension of nanoparticles was maintained under magnetic stirring at 100 rpm and room temperature for 30 min. CS/PEG nanoparticles were prepared by adding 10 mg of PEG 8000 to each mL of the earlier prepared CS solution under magnetic stirring at 200 rpm for 30 min, before the dripping of TPP, as previously described [47]. Finally, I3C-loaded nanoparticles were formed by the addition of different concentrations of indole-3-carbinol (12 to 80 μM) to chitosan or chitosan/PEG solutions under magnetic stirring at 100 rpm for 30 min at 25 °C before the incorporation of TPP solution (Fig. 1). The samples were lyophilized to obtain solid particles or stored at 4 °C in their natural form.

2.2.3. Determination of encapsulation efficiency (EE)

Nanoparticles containing I3C were centrifuged at 10,000 x*g*, 4 °C for 1 h in a Rotina 380 R Benchtop centrifuge (Andreas Hettich GmbH & Co. KG - Tuttlingen, Germany). *EE*, defined as the amount of drug associated with the nanoparticles, was determined (Eq. (1)):

$$EE\ (\%) = \left(\frac{I3C_o - I3C_f}{I3C_o}\right) \times 100 \quad (1)$$

where $I3C_o$ is the concentration of total drug offered during the encapsulation process and $I3C_f$ represents the free drug present in the dispersion supernatant, determined after centrifugation. The quantification was performed on a spectrophotometer (280 nm), and the I3C concentration was estimated through the previously established standard curve.

2.2.4. Particle size, polydispersity index, and zeta potential

Mean size and polydispersity index (PDI) of the nanoparticles were measured by Dynamic Light Scattering (DLS) technique using a Malvern Zetasizer Nano S (Malvern Instruments, Worcestershire, UK). An aliquot (1 mL) of nanoparticle solutions was added in polystyrene cuvettes and the analysis was carried out at a scattering angle of 90° at 25 °C. Additionally, samples at pH 5.0 were loaded into a capillary cell and analyzed at 25 °C in order to measure their surface charge by Zeta Potential (ZP). The results were reported as an average value ($n = 6$) for both techniques.

2.2.5. Scanning electron microscopy (FEG-SEM)

Morphological properties of the nanoparticles were evaluated by Field Emission Gun Scanning Electron Microscopy (FEG-SEM), using an Inspect F50 microscope (FEI Company - Tokyo, Japan). Liquid samples were dropped on carbon tape covered aluminum stubs, dried at 40 °C for 2 h, sputtered in the secondary electron mode (gold metallization), and analyzed at 20 kV.

2.2.6. Fourier-transformed infrared spectroscopy (FTIR) analysis

FTIR analysis was performed using a Cary 630 Spectrophotometer (Agilent Technologies – California, USA), equipped with a zinc selenide crystal (ZnSe) and an ATR (total attenuated reflection) device. About 2 mg of the lyophilized samples were added on the crystal surface in a spectral range of 4000 to 650 cm^{-1}, under resolution of 2 cm^{-1}, and the processed data was automatically acquired using the Agilent MicroLab PC software.

2.2.7. X-ray powder diffraction (XRD) analysis

In order to evaluate the crystallinity pattern of the materials, the pure compound and the lyophilized polymeric nanoparticles obtained were evaluated in an X-ray diffractometer model MiniFlex II (Rigaku - Tokyo, Japan), operated in conventional 2θ geometry, with analysis angle between 1.35 and 70 degrees, scan rate of 5°/minute, and voltage of 30 mA. Copper radiation was used as the source, with λ = 1.54 nm. The crystallinity fraction (Xc) is calculated from the area of crystalline peaks (Ac) and the total area of amorphous and crystalline peaks (At), following the Eq. (2) [48]:

$$Xc\ (\%) = \left(\frac{Ac}{At}\right) \times 100 \quad (2)$$

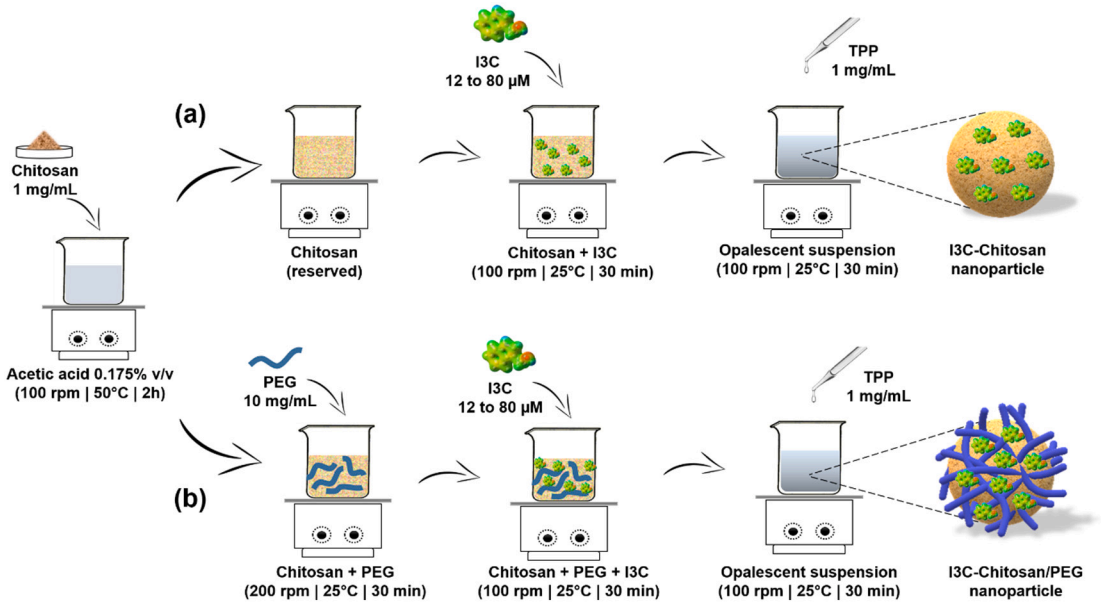

Fig. 1. Schematic representation of the step-by-step preparation of (a) I3C-CS nanoparticles, and (b) I3C-CS/PEG nanoparticles.

2.2.8. Thermal analysis

Thermogravimetric analysis (TGA) was carried out using an SDT equipment model Q600 (TA Instruments – Delaware, USA). About 5.0 mg of the samples were supported in an alumina crucible and analyzed using a flow rate of 10 mL/min, under inert nitrogen and heating flow of 10 °C/min, from 35 °C to 500 °C. Differential scanning calorimetry (DSC) was performed through the DSC-50 cell (Shimadzu - Kyoto, Japan), with a flow rate of 50 mL/min, under inert nitrogen, and heating rate of 10 °C/min from 35 to 500 °C. Samples (2.0 mg) were analyzed in closed aluminum capsules and an empty aluminum capsule was used as reference.

2.2.9. In vitro release assay

The *in vitro* release of I3C from CS and CS/PEG nanoparticles was performed using the dialysis membrane diffusion method. Approximately 10 mL of the nanoparticles were placed into a dialysis bag (5 cm length, 25 mm flat width and 16 mm in diameter, 14,000 MWCO - InLab, Brazil) which was immersed in a beaker containing 90 mL of phosphate buffer solution simulating the tumor periphery (pH 5.5) at 37 ± 1 °C, under magnetic stirring of 200 rpm. At programmed intervals (0, 0.5, 1, 2, 3, 6, 9, 12, and 24 h), a volume of 1 mL of the release medium was collected, added in 2 mL of phosphate buffer and analyzed in a UV–Vis spectrophotometer at a wavelength of 280 nm. The same volume of fresh buffer solution at the same temperature was added immediately to maintain a constant release volume. The cumulative release (CR) percentage of I3C was determined from the Eq. (3):

$$CR\ (\%) = \left(\frac{I3C_t}{I3C_i}\right) \times 100 \tag{3}$$

where $I3C_t$ is the amount of drug released at the time t and $I3C_i$ is the initial amount of drug encapsulated in the NP. The tests were carried out in triplicate for both formulations.

The *in vitro* drug release data of the nanoparticles were fitted to five kinetic models *i.e.*, zero order, first order, Korsemeyer–Peppas, Higuchi's square root plot, and Hixson-Crowell cube root plot, selecting the most appropriate model based on the obtained R^2 values. The diffusion exponent (*n*) was calculated from the slope of the plot obtained through the Korsmeyer-Peppas model in order to determine the release mechanism.

2.2.10. Computational details

To evaluate the quantum properties of I3C molecule, as well as, to study the possibilities of the interaction of I3C with PEG or chitosan, a computational study was performed using Density Functional Theory (DFT) calculation. The geometrical structures optimization was performed without any constraint using ωB97-XD functional in combination with 6–311++G(d,p) basis set, as implemented in the GAUSSIAN 16 package. The frontier orbital energies were calculated in single point runs at the same theory level. Molecular electrostatic potential maps (MEPs) of total electronic densities using the partial charges were analyzed with Gabedit software [49], with an isosurface value of 0.014181 and grid values from −0.1 to 0.1. To perform non-covalent interaction (NCI), we have utilized Multiwfn code developed by Lu and Chen [50]. The 2-D isosurface plot for reduced electron reduced gradient was plotted by VMD software [51].

2.2.11. Cell culture and maintenance

Human bladder cancer cell line (T24) (American Type Culture Collection – Rockville, MD, USA) was maintained in RPMI-1640 culture medium, supplemented with 10% (*v*/v) fetal bovine serum (FBS), 0.5 U/mL of penicillin and streptomycin antibiotics, and 0.1% (v/v) fungizone. Cells were maintained in a humidified cell incubator (37 °C, 5% CO_2 atmosphere, and 95% relative humidity) until the experiment, and were lifted from the subconfluent cultures with 0.5% trypsin in 5 mM EDTA, counted on a hemocytometer, and plated at the appropriate density according to the experimental protocol.

2.2.12. Preparation of I3C and I3C-loaded nanoparticles for treatment

I3C solution was suspended in RPMI-1640 culture medium at a concentration of 2000 μM and serially diluted in different concentrations (25, 50, 100, 250, 500, 750, 1000, and 1500 μM). I3C-loaded nanoparticle solutions were concentered by centrifuging at 5000 x *g* in different spin times using an Amicon® Ultra-15 Centrifugal Filter with a molecular weight cutoff of 100 kDa and suspended in RPMI-1640 culture medium in order to obtain the appropriate final concentrations (100, 200, 300, 400, 500, 750, and 1000 μM). The encapsulation efficiencies of nanoparticles were considered as the correction factors.

2.2.13. Cell viability by MTT assay

Cell viability was determined by the Methyl-thiazolyl-tetrazolium (MTT) colorimetric assay for metabolic activity since the amount of formazan crystals produced is proportional to the number of metabolically active cells [52]. T24 cells were seeded at a density of 5×10^3 cells/well in a 96-well plate, with 100 μL of RPMI-1640 culture medium. After confluence, cells were treated with different concentrations of free I3C, I3C-CS NP, and I3C-CS/PEG NP, as previously determined, and incubated for 24 h. Cells treated only with the medium was considered as a control experiment and pure nanoparticles were used for comparative purposes. After the treatment period, the medium was removed, the cells were washed with PBS (pH = 7.3 ± 0.1), added with 100 μL of MTT, and incubated for 3 h. After incubation, formazan crystals were dissolved in 100 μL of dimethyl sulfoxide (DMSO), and optical density was measured in an automated Victor X3 plate reader (PerkinElmer - Waltham, Massachusetts, USA) at 570 nm wavelength. Absorbance was linearly proportional to the number of live cells with mitochondrial activity. Three independent experiments were performed for each concentration, all of these in triplicate. The results were determined as a percentage of the absorbance of treated cells in relation to the control group and were calculated as Eq. (4):

$$Cell\ Viability\ (\%) = \left(\frac{A_{sample}}{A_{control}}\right) \times 100 \tag{4}$$

where A = absorbance at 570 nm.

The values of half of the maximum inhibitory concentration (IC_{50}), defined as the concentration of the drug capable to inhibited cell viability by 50%, for free I3C, I3C-CS NP, and I3C-CS/PEG NP were calculated by measuring the activity by the correlation between the percentage of cell viability and the concentration logarithm.

2.2.14. Statistical analysis

The experimental data were expressed as the mean ± standard error of the mean (S.E.M.) or represented as error bars in figures. Differences between the experimental groups were analyzed for statistical significance by one-way or two-way analysis of variance (ANOVA) followed by Tukey or Bonferroni post-hoc tests, respectively, using the Prism GraphPad Prism® 7.0 (Intuitive Software for Science, San Diego, CA, USA). Significant values were set at $p < 0.05$ (*** $p < 0.001$; ** $p < 0.01$; * $p < 0.05$).

3. Results and discussion

3.1. Preparation of nanoparticles and encapsulation efficiency of I3C

All prepared formulations showed an opalescent characteristic and no particulate aggregates were observed after the crosslinking of the chitosan and chitosan/PEG solutions with TPP, which indicates the process of formation of nanoparticles by ionic gelation was obtained successfully (Calvo, Alonso, & Remun, 1997). The loading study of the I3C on nanoparticles was carried out in the range of 12 to 80 μM. To determine the incorporated fraction, the Encapsulation Efficiency (*EE*)

was performed and the I3C concentrations were measured from the calibration curve previously obtained (y = 4.8969×; R^2 = 0,99,938). The *EE* values growth according to the increase in the I3C concentration, reaching 79.4% for the CS nanoparticles and 78.7% for the CS/PEG nanoparticles in the highest drug loading (80 μM), according to Fig. 2. Based on this finding, we suggest that the presence of PEG does not directly affect the I3C encapsulation efficiency, and the formulations with the highest encapsulation efficiencies were chosen for characterization and other experiments.

Some studies have encapsulated indole-3-carbinol in different types of particles [24–27,53,54]. Luo et al. (2013) obtained 63% *EE* in zein nanoparticles and 77% in zein nanoparticles coated with carboxymethyl chitosan from 50 μg/mL of the drug [54]. Song et al. (2014) obtained 7.9% *EE* of I3C in liposomes [26]. Gehrcke et al. (2018) obtained 41% and 42% *EE* for I3C encapsulated in rosehip oil nanocapsules and medium-chain triglyceride nanocapsules, respectively [24]. In comparison with studies that used the same biomolecule in other nanocarriers, the results presented in this work suggest a satisfactory encapsulation efficiency of indole-3-carbinol in both chitosan and chitosan/PEG nanoparticles.

We hypothesize that encapsulation occurs due to the physical confinement of I3C in the interstices of nanostructured material by the gelation process, associated to the occurrence of hydrogen bonding between the drug and the polymers. It is possible due to the presence of the NH and OH donor groups of the indole compound, capable to establishing interactions with the polymeric matrix, reinforcing its fixation to the nanomaterial [23].

3.2. Particle size, polydispersity index and zeta potential of nanoparticles

In order to evaluate the nanometric characteristics of materials, the average size (nm), IPD, and PZ values for the pure and I3C-loaded CS, CS/PEG nanoparticles were obtained, and the results are presented in Table 1.

Pure chitosan nanoparticles were found at 133.3 ± 3.7 nm and its surface charge was measured at +24.3 ± 0.5 mV. In its turn, Chitosan/PEG nanoparticles increase their size to 169.2 ± 2.0 nm and decrease the positive charge to +20.9 ± 0.3 mV. The increase in the average diameter and the reduction of the particle charge after the addition of PEG are in line with the literature [41] and in agreement with our previous work [47]. Chitosan nanoparticles had an increase in the average diameter to

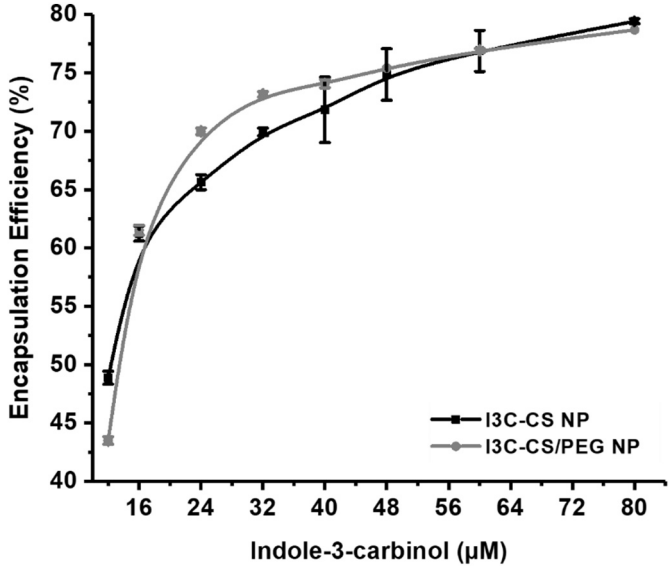

Fig. 2. Encapsulation efficiency of I3C into chitosan and chitosan/PEG nanoparticles as a function of concentration (12 to 80 μM).

Table 1
Summary of size, PDI, zeta potential, and encapsulation efficiency values for chitosan and chitosan/PEG nanoparticles loaded with I3C (n = 6).

Sample	Size (nm)	PDI	Zeta potential (mV)	*EE* (%)
CS NP	133.3 ± 3.7	0.26 ± 0.02	+24.3 ± 0.5	–
I3C-CS NP	165.5 ± 2.5	0.37 ± 0.05	+23.1 ± 0.6	79.4 ± 0.2
CS/PEG NP	169.2 ± 2.0	0.32 ± 0.03	+20.9 ± 0.3	–
I3C-CS/PEG NP	180.4 ± 2.7	0.37 ± 0.01	+20.3 ± 0.5	78.7 ± 0.1

165.5 ± 2.5 nm after I3C incorporation in a significant manner ($p < 0.001$). The values suggest that the presence of the drug offers an increase of about 32 nm in the average size of the nanoparticles. The ZP values of the CS NP containing I3C was 1.2 mV lower than the pure particle (+23.1 ± 0.6 mV). In addition, I3C-loaded chitosan/PEG nanoparticles presents an increase in the average diameter by about 10 nm (180.4 ± 2.7 nm) ($p < 0.001$), with a slight decrease of 0.6 mV in the surface charge (+20.3 ± 0.5 mV) in comparison to CS/PEG nanoparticles. All particles show a polydispersity index between 0.26 and 0.37, indicating a relatively homogeneous dispersion of nanoparticles [55] and ZP higher than +20 mV, indicating moderate stability [56]. PDI and ZP values of I3C-loaded nanoparticles did not present statistical significance when compared to pure nanoparticles.

Scheeren et al. (2016) obtained similar results in the encapsulation of doxorubicin in chitosan and chitosan/PEG nanoparticles, where was observed an increase in the mean diameter of ~20 nm and ~ 15 nm after drug incorporation in the chitosan and chitosan/PEG nanoparticles, respectively [41]. Gehrcke et al. (2018) obtained an increase of 13 nm in the average diameter of oil nanocapsules after incorporation of I3C. These results reinforce the hypothesis that the increase in size of the particle after the addition of indole-3-carbinol indicate the effective encapsulation of this molecule on CS and CS/PEG nanoparticles [24].

Physicochemical characteristics, such as particle size and surface charge properties, played fundamental roles in the cellular absorption of polymeric nanoparticles. It is known that nanoparticles presenting sizes close to 150–200 nm are prone to permeate vasculature of tumor tissues, passively accumulate due to enhanced permeability and retention effect (EPR) and undergo cell internalization by non-phagocytic cells through nonspecific endocytosis [57,58]. In addition, positively charged nanoparticles increase the percentage of cell absorption, once the positive surface charge of the particle promotes a stronger affinity for the negatively charged cell membrane, favoring their greater cellular absorption [38].

3.3. Morphology study of nanoparticles by SEM

Scanning electron microscopy was used to characterize the morphology of chitosan and chitosan/PEG nanoparticles after I3C encapsulation (Fig. 3). I3C-CS nanoparticles (Fig. 3a) are mostly spherical, ragged, and demonstrate a little dispersed average diameter distribution. I3C-CS/PEG NP (Fig. 3b) are also spherical in shape, but presents a smooth surface without aggregation, indicating an important capping strength of the PEG. This observation is in accordance with other authors [59,60], and may be explained due to the fact of PEG introduces a hydrophilic shell based on several polyoxyethylene groups around of NP [61].

The spherical shape of these nanoparticles indicates an effective interaction between the reactive groups of the formulation components, while the size of the nanoparticles in a range of 150–250 nm (individual measurement are not shown) represents an important factor to reach the tumor environment [62]. Thus, the morphologic analysis proved that both nanoparticles are good candidates for a drug delivery system in cancer therapy in terms of physical structure and their sizes are in agreement with DLS results presented previously in this work.

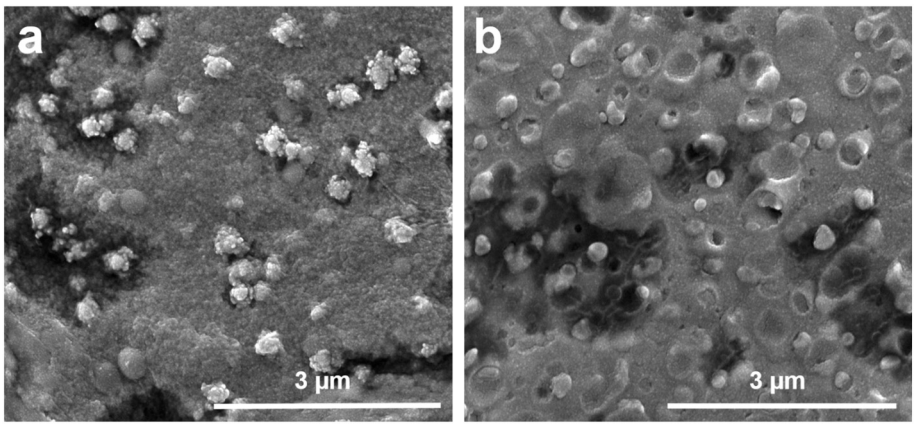

Fig. 3. Photomicrographs by SEM (50,000× magnification) of (a) I3C-CS NP and (b) I3C-CS/PEG NP.

3.4. FTIR spectra

Chemical structures of I3C and the prepared nanoparticles were analyzed by FTIR spectroscopy and can be seen in Fig. 4a. In the I3C spectra, characteristic bands of the indole ring are seen at 739 cm^{-1}, corresponding to the out of plane deformation vibration of C—H [23]. The bands at 1453 cm^{-1} and 1543 cm^{-1} are attributed to the aromatic C═C bonds of indole ring [24,45]. It is also possible to observe weak bands at 2860 and 3052 cm^{-1} corresponding to the CH stretching of alkyl groups (–CH, $–CH_2$ and $–CH_3$), and at 3090 cm^{-1} for aromatic stretching [53]. Finally, the OH and N—H (secondary amine bond) stretching range at 3378 cm^{-1} [24,45].

After loading I3C on CS NP, no characteristic peak of I3C appears in the encapsulated NP spectrum. Valderrama et al. (2020) also observed similar find after encapsulating another indole compound in CS nanoparticles. The authors attributed this occurrence due to the small amounts of loaded compound or due to the fact that the compound is dispersed in the polymeric matrix of the nanoparticle, resulting in an exclusive observation of the CS NP spectrum profile [63]. However, the band between 3600 cm^{-1} and 3000 cm^{-1} corresponding to the OH stretching vibration increases in comparison with pure CS NP (Fig. 4b), possibly due to a new intermolecular interaction by hydrogen bond

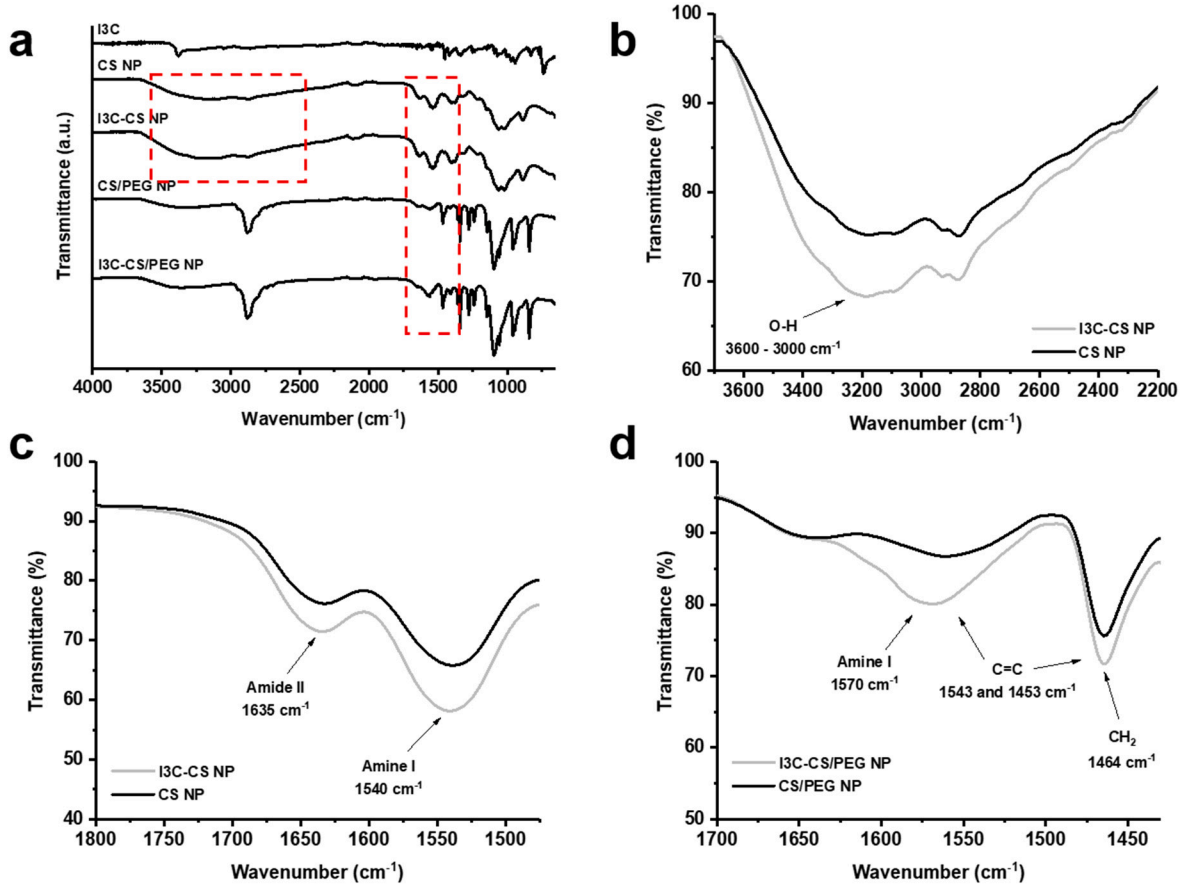

Fig. 4. FTIR spectra of I3C, chitosan nanoparticles (CS NP), I3C-loaded chitosan nanoparticles (I3C-CS NP), chitosan/PEG nanoparticles (CS/PEG NP), and I3C-loaded chitosan/PEG nanoparticles (I3C-CS/PEG NP) (a); Comparing the FTIR spectra of CS NP and I3C-CS NP between 3700 and 2200 cm^{-1} (b), and 1800–1450 cm^{-1} (c); and FTIR spectra of CS/PEG NP and I3C-CS/PEG NP between 1700 and 1430 cm^{-1} (d).

formed between I3C and chitosan [64]. In addition, the chitosan bands of amine I (1540 cm^{-1}) [65] and amide II (1635 cm^{-1}) [66] were more pronounced in the spectrum of I3C-loaded nanoparticles, when compared to the pure nanoparticles (Fig. 4c), which suggests the interaction between the indole compound and chitosan. The increase of the amine I band of chitosan (1570 cm^{-1}), in addition to the increase in the vibration band intensity of CH_2 from PEG at 1464 cm^{-1} [67], may indicate the overlap of the aromatic vibration of C═C from I3C (1453 cm^{-1} and 1543 cm^{-1}) in the spectrum of I3C-CS/PEG nanoparticles (Fig. 4d). These changes can suggest the presence of I3C and reflect the physical entrapment of the indole compound in both chitosan and chitosan/PEG nanoparticles.

3.5. XRD analysis

The X-ray diffraction patterns of I3C, CS NP, CS/PEG NP, and these nanoparticles after I3C encapsulation are shown in Fig. 5. The diffraction patterns of the CS NP show two characteristic peaks at 19.1° and 22.5°. Such peaks can be indexed as chitosan fractions [68]. Other peaks at 11.45°, 29.70°, and 44.60° are attributed to the presence of TPP [69]. In addition, CS NP presented a crystallinity of 21%, characteristically more crystalline than pure CS [48], as a result of the ionic interaction between TPP and $-NH_3^+$ of chitosan molecules, transforming amorphous chitosan into a crystallized form [70]. On the other hand, CS/PEG NP shows strong peaks at 19.10° and 23.25°, and weaker peaks at 26.10°, 30.85°, 36.15°, and 39.70°, characteristic of PEG [71]. After adding PEG, the crystallinity of the nanoparticle increases from 21% to 50%. This observation can be attributed to the inherent high crystalline structure of the PEG molecules [72].

The main characteristic peaks of I3C were observed at 5.7°, 11.35°, 17.05°, and 34.25°, attributed to its highly crystalline state, which was consistent with the literature [24,54]. After encapsulation in both nanoparticles, the peaks attributed to I3C were not observed. However, the crystallinity degree of both nanoparticles increased after I3C addition (43% to I3C-CS NP and 57% to I3C-CS/PEG NP). These results indicated that the crystalline structure of I3C was incorporated into the nanoparticles, providing additional evidence of encapsulation by the molecular dispersion of I3C in the nanoparticles [24,54].

Has been known that the use of phytochemicals (as is the case with indole compounds) in the process of preparing chitosan nanoparticles results in the suppression or reduction of diffraction peaks characteristic of the crosslinked polymer due to the amorphization process resulting from the presence of these molecules in the crystalline network of the polymer [62]. In this way, XDR results are in accordance with the FTIR description for I3C-loaded nanoparticles in this work.

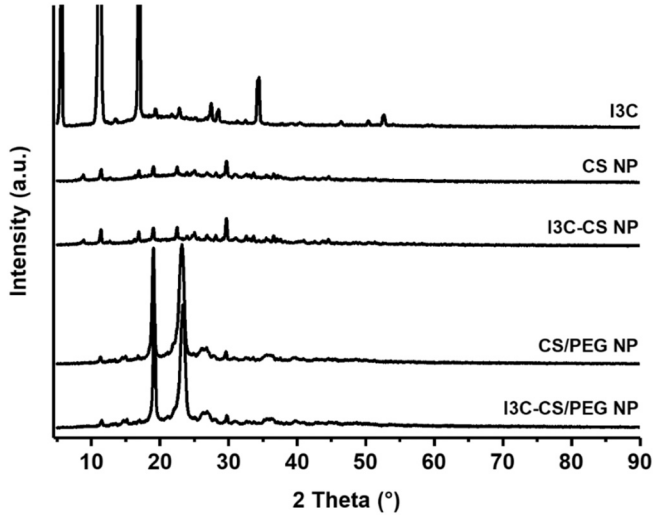

Fig. 5. X-ray diffraction patterns of I3C, chitosan nanoparticles (CS NP), I3C-loaded chitosan nanoparticles (I3C-CS NP), chitosan/PEG nanoparticles (CS/PEG NP), and I3C-loaded chitosan/PEG nanoparticles (I3C-CS/PEG NP).

Similar results were obtained by Maity et al. (2017) during the study of naringenin encapsulation in chitosan/alginate core-shell nanoparticles, and by Balaji, Raghunathan, & Revathy (2015) in the encapsulation of levofloxacin in alginate-chitosan nanoparticles, which state that an XRD signal from encapsulated drugs becomes very difficult to detect [73,74]. Thus, it is possible to consider that the disappearance of the drug peaks in the nanoparticles is a clear indication of the dispersion at the molecular level of the drug within the nanoparticle matrix [75].

3.6. Thermal analysis

Fig. 6a and b summarize the TG/DTG curves of CS NP and CS/PEG NP before and after loading I3C. TG thermograms of CS NP before and after I3C encapsulation (Fig. 5a) presents a similar decomposition behavior within three transition states. The first stage up to 200 °C is attributed to physically adsorbed humidity. The second stage occurs from 200 °C to 350 °C and can be attributed to the thermal decomposition of the pyranose ring of chitosan. The third decomposition stage may be shown between 350 °C and 500 °C and indicates the decomposition of adducts [76,77]. However, an increase in the intensity of the T_{peaks} at 135 °C, 265 °C and 460 °C for I3C-CS NP compared to the pure nanoparticle can be shown.

Fig. 6b points to a progressive weight loss is observed in CS/PEG NP from 200 °C to 350 °C, attributed to the decomposition of organic components. Despite presenting a similar decomposition profile, I3C-CS/PEG NP showed less loss of mass in the same temperature range. It may indicate an increase in thermal stability after the addition of the drug. After that, a substantial weight loss between 350 °C and 420 °C indicating to the pyrolysis of PEG functional groups may be observed [78]. Furthermore, the appearance of a new T_{peak} at 250 °C and a considerable increase in the intensity at 410 °C for I3C-CS/PEG NP can also be observed. Finally, in both cases, the residual mass was lower for the I3C-loaded nanoparticles (1.44% less than CS NP, and 3.96% less than CS/PEG NP), indicating that the difference of total weight loss can confirm the decomposition of the drug. These results are compatible with the process of thermal degradation of the indole ring described previously [79,80] and point to the drug encapsulation in both nanoparticles.

DSC curves of I3C, CS NP, CS/PEG NP, and I3C-loaded NPs are summarized in Fig. 6c. Pure I3C showed an endothermic event at 88 °C, which corresponds to its melting temperature and an exothermic decomposition event at 423 °C. The nanoparticles containing I3C showed an overlap of the thermal events, especially between 50 °C and 65 °C, attributed to the nature of the pure nanoparticles and the drug, despite presenting them in less intensity, which indicates the occurrence of amorphization of the I3C [24]. In addition, the occurrence of a new exothermic decomposition event at 392 °C for the I3C-CS NP, not observed to the pure CS NP, and the change and expansion of an exothermic event from 405 °C (CS/PEG NP) to 416 °C (I3C-CS/PEG NP) suggest the pyrolysis process of the indole ring [81], indicating the presence of I3C in these nanomaterials. Thus, these events are compatible with the thermal decomposition profiles observed by TGA in this work, reinforcing the argument of the I3C encapsulation in both nanoparticles.

3.7. In vitro release

The release of drugs from biodegradable polymeric particles follows numerous mechanisms, such as the desorption of the particle surface, degradation, and erosion of the polymer, diffusion, and reabsorption through the pores of the polymer network [62]. The *in vitro* release assay for the CS and CS/PEG nanoparticles containing I3C was carried out at pH 5.5 in order to mimic the tumor microenvironment and had a

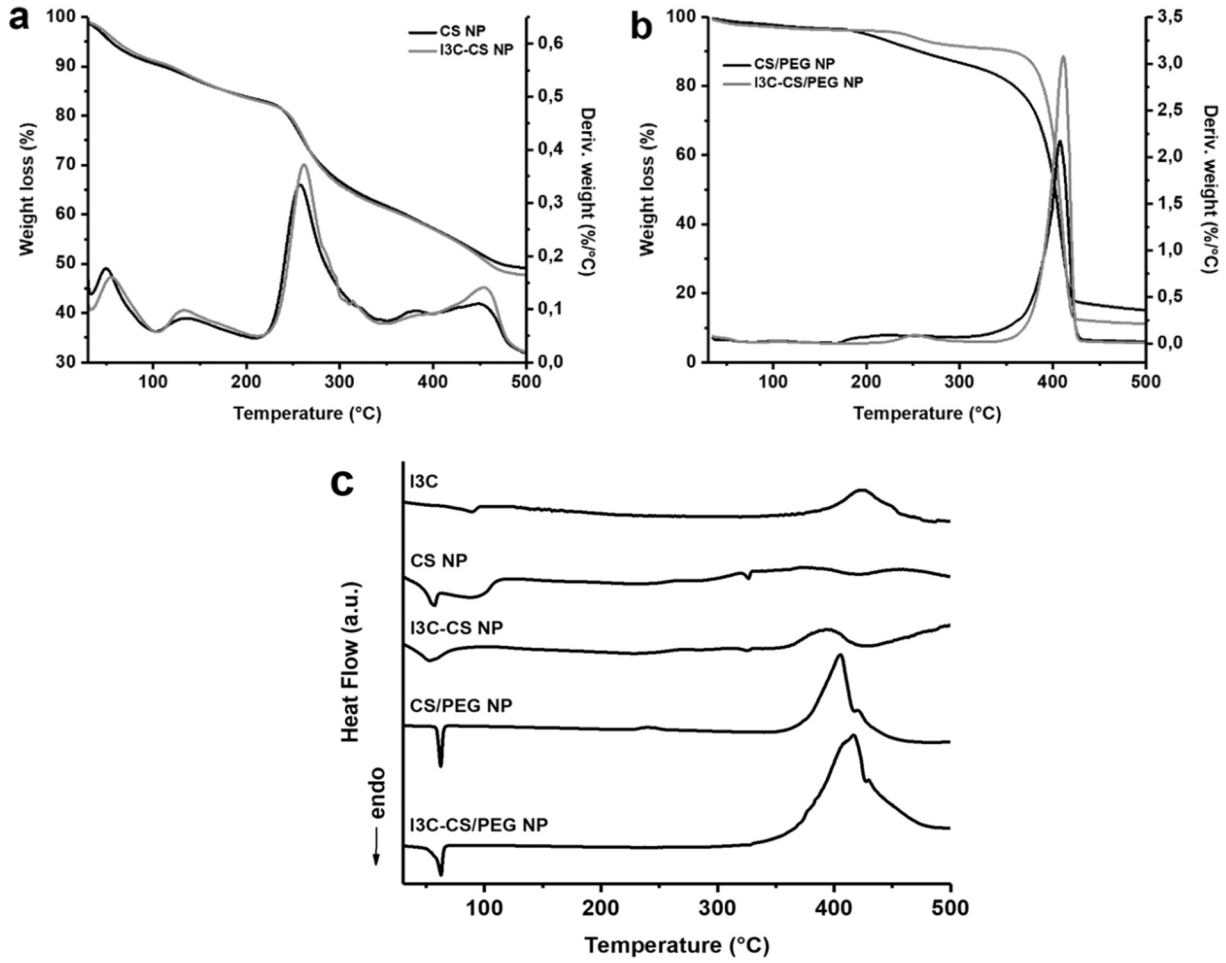

Fig. 6. Thermogravimetric and Derivative Thermogravimetric profiles of (a) CS NP and I3C-CS NP; and (b) CS/PEG NP and I3C-CS/PEG NP; (c) DSC spectra of I3C, CS NP, I3C-CS NP, CS/PEG NP and I3C-CS/PEG NP.

maximum duration of 24 h. The graph that represents the release profiles can be analyzed in Fig. 7.

As for the effect of the I3C release, chitosan nanoparticles showed 64% release after 3 h, while the CS/PEG nanoparticles managed to release 60% of the drug in the same time. By the end of the experiment, I3C-CS NP reached 88% release, compared to approximately 76% of I3C-CS/PEG NP. Thus, the presence of a pattern of bimodal release of I3C with high initial burst release followed by a slow-release pattern can be considered. A two phases profile was also attributed to other nanomaterials [82].

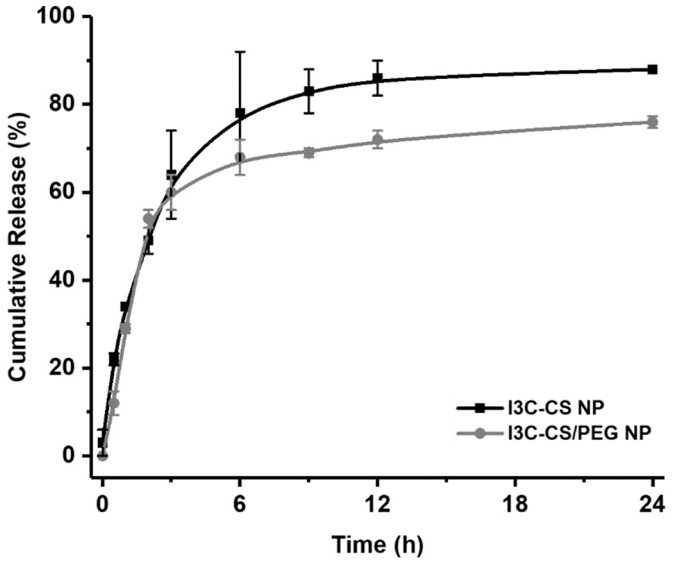

Fig. 7. Cumulative release profiles for I3C-CS NP and I3C-CS/PEG NP at pH 5.5.

In agreement with our findings, Luo et al. (2013) observed a high release of I3C from zein nanoparticles coated or not with carboxymethyl chitosan (40% and 50%, respectively) during the first 30 min, followed by a sustained release up to 6 h of experiment. For the authors, the coating with carboxymethyl chitosan helped to reduce the immediate release of the drug, stating that the coating promotes an improvement in the release profile of compounds in nanoparticles [54].

The release profiles of nanoparticles were analyzed by zero order and first order kinetics, Higuchi, Korsmeyer-Peppas, and Hixson-Crowell models. The obtained correlation coefficients (R^2) are presented in Table 2. Higuchi model appeared to be the best fit among the five models for I3-CS NP, with the R^2 value of 0.9852, indicating that the diffusion process pays an important role on the release mechanism of I3C from these particles [83]. The Higuchi model was also observed for many authors using chitosan nanoparticles as carrier for different types of molecules [84–86].

On the other hand, the presence of PEG changes the release profile of I3C. In this case, the Korsmeyer-Peppas model was best fitted as a release kinetic of I3C from CS/PEG nanoparticles (R^2 = 0.9803), which indicates that the relaxation of the polymer chains also contributes in the

Table 2
Release model analysis of I3C-CS NP and I3C-CS/PEG NP based on *in vitro* release experiment data[a].

Release model	Model equation	I3C-CS NP		I3C-CS/PEG NP	
		R^2 value	*n*-value	R^2 value	*n*-value
Zero order	M_0-$M_t = kt$	0.8625	–	0.7642	–
First order	$\ln M_t = \ln M_0 + kt$	0.9693	–	0.8506	–
Higuchi	M_0-$M_t = kt^{1/2}$	0.9852	–	0.9202	–
Korsmeyer-Peppas	$\log (M_0$-$M_t) = \log k + n \log t$	0.9785	0.7647	0.9803	0.7646
Hixon-Crowell	$M_0^{1/3}$-$M_t^{1/3} = k_s t$	0.9341	–	0.8222	–

[a] M_0 represents the initial drug amount; M_t indicates the amount of drug remaining at a specific time; k means the rate constant; t refers to the time; n is the diffusion exponent.

release mechanism [87]. In addition, nanoparticles containing PEG showed a slower release rate compared to nanoparticles without this polymer, corroborating the behavior described above. In agreement with the observed in this study, Elwerfalli et al. (2015) also concluded that chitosan nanoparticles coated with PEG showed a slower release profile of promethazine compared to uncoated ones [88].

Furthermore, the Korsmeyer-Peppas equation is able to define the mechanism of drug release, which can be evaluated by n-value. When $n = 0.43$, the release is described as Fickian diffusion, where the material does not suffer relevant deformation or stresses during drug release. Additionally, the release is through anomalous diffusion (non-Fickian diffusion) if $0.43 < n < 0.85$, where there may be swelling or stress of the polymer during drug release. Finally, when $n > 0.85$, there is a Case II transport, where the drug release could be purely due to polymer swelling [89].

The I3C release mechanism resulted in similar release exponents (n) for I3C-CS NP and I3C-CS/PEG NP (0.7647 and 0.7646, respectively), observed in Table 2. These results indicate that both nanoparticles exhibited release by anomalous transport, being in agreement with the release kinetics profile. This behavior may indicate that during the first hours, the molecules attached to the surface of the nanoparticles could separate and be transferred to the release solution, while the molecules trapped inside the nanoparticles were released gradually. This release profile may be attributed to the progressive swelling of PEG and the decomposition of chitosan at this pH, reinforcing the hypothesis that the active molecule is released efficiently in the tumor environment [62].

3.8. Computational characterization

The interactions between I3C molecules and the chitosan or PEG can occur, as observed in the results addressed so far, by hydrogen bonds involving OH or NH groups from I3C. To evaluate this interaction, as well as describe some quantum properties of I3C molecules, which is scarce in the literature, a computational study was realized. To gain a deeper insight into the quantum properties of I3C, electrostatic potential (MEP) and Frontier molecular orbital (FMO) were calculated. Both these analyses given indicative of the electrophilic or nucleophilic behavior of a molecule. MEP simultaneously displays molecular shape, size, and electrostatic potential in terms of color grading. The FMO results provide knowledge about the electronic properties and the energy gap between the HOMO and LUMO of the molecules. The HOMO (Highest Occupied Molecular Orbital) can be considered the outermost orbital containing electrons, characterizes the ability to donor electron, while LUMO (Lowest Unoccupied Molecular Orbital) considered the innermost orbital containing free places to accept electrons [90,91].

The result of MEP to I3C is presented in Fig. 8a and the potential increases in the order red < orange < yellow < green < blue. According to the color scale, the red color present indicates nucleophilic domains, while the blue color represents an electrophilic character [92]. As observed, the unique nucleophilic center presented in the I3C molecule is the oxygen atom that has the negative potential in their around, while its observed three potential electrophilic centers that are the hydrogen atoms bonded to nitrogen, to the carbon neighbor of nitrogen and the most electrophilic is hydrogen-bonded to the oxygen atom, been acid hydrogen.

In the interaction of molecules, the two main responsible orbitals are generally the HOMO of one molecule and the LUMO of another molecule. The results related to FMO are presented in Fig. 8b and c, where the red color indicates the negative phase, while the blue color indicates the positive phase. The HOMO of the I3C molecule is uniformly distributed along the molecule, except around the OH group. The LUMO orbital is shifted towards NH and OH groups of the molecule, which corroborated with the MEP results, where the hydrogen-bonded to N and O has the positive potential around, been a possible stronger point of interaction. The HOMO-LUMO energy gap for a single molecule indicates the stability through the lowest electronic excitation energy, corresponding to the lowest excitation [93]. Thus, the lower values of the energy gap indicate low stability. The HOMO–LUMO energy gap explains the eventual charge transfer interaction within the molecule, which

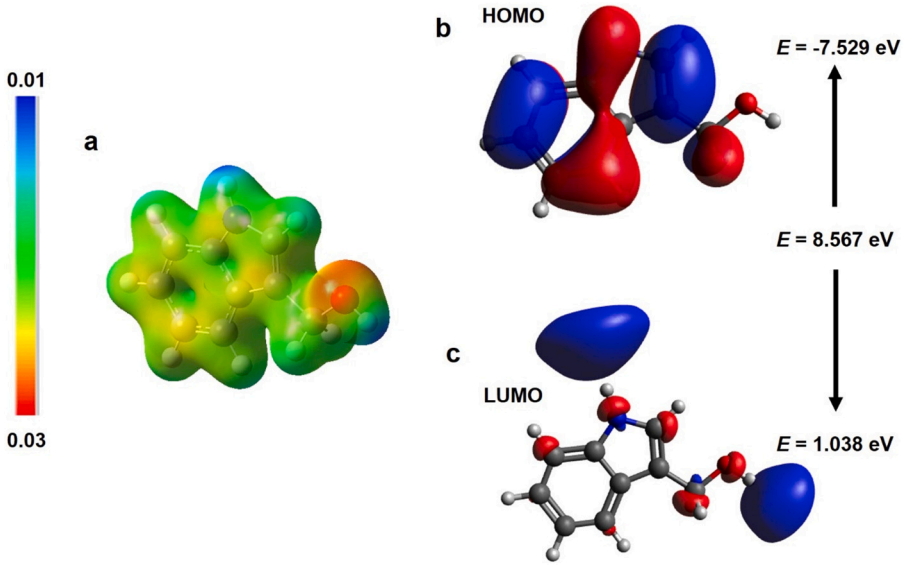

Fig. 8. Results of (a) Molecular electrostatic potential, (b) HOMO, and (c) LUMO Frontier molecular orbital of I3C molecule.

influences the biological activity of the molecule. The value of I3C was 8.567 eV, indicating that I3C can be considered a molecule with good stability.

The HOMO-LUMO energy gap is indicative of the electron-donating and receiving ability of a molecule [94], and a lower value generally is associated with a high chemical reactivity, low kinetic stability, and highly polarizable. Besides these, using the value of the HOMO-LUMO energy gap, it is possible obtained important global reactivity descriptors such as chemical hardness (η), global softness (S), and chemical potential (μ) that provide information about the stability and chemical reactivity of a molecule, described by the following Eqs. (5), (6), and (7):

$$\eta = \frac{1}{2}\,(\epsilon\mathrm{LUMO} - \epsilon\mathrm{HOMO}) \tag{5}$$

$$S = \frac{1}{2\eta} \tag{6}$$

$$\mu = \frac{1}{2}(\epsilon\mathrm{HOMO} + \epsilon\mathrm{LUMO}) \tag{7}$$

The results of global reactivity descriptors were calculated in the gas phase. Hardness fundamentally signifies the resistance towards the deformation or polarization of the electron cloud of the atoms, ions, or molecules under small perturbation of chemical reaction [95]. The values of hardness and softness were 4.2835 and 0.1167 eV, respectively, indicating that I3C is a hard than a soft molecule, which mean it is stable and has no trend to transfer charge because it resist changes in their electron number and distribution [93,96]. The chemical potential (μ) describes the escaping tendency of electrons from an equilibrium system. Higher values indicated that the compound is less stable or more reactive. As observed, the value of I3C is −3.2455, which can be considered a higher value, corroborating the results of hardness, which indicated good stability of the molecule.

The reduced density gradient (RDG) and non-covalent interaction (NCI) are a powerful means to study the inhomogeneous electron distribution at the non-bonding regions of the substrates [97]. The results of RDG (Fig. 9a and b) of both systems (*i.e.* I3C/chitosan and I3C/PEG) is characterized by the presence of three regions. The first one is a region with a positive λ2, indicating a contribution of weak repulsive interactions, been similar for both systems. The second region is characterized by values of λ2 close to neutral corresponding to weak attractive interactions, which are of van der Waals type. In the case of I3C/chitosan, this interaction has a greater contribution when compared with I3C/PEG. The last region presenting a negative λ2, which indicates strong attractive interactions [98], and both systems possess a similarity of this contribution. This find is reinforced by the results of FTIR analysis (Fig. 4), where is observed an increase in the OH stretching vibration, being able to indicate a new inter-molecular interaction.

NCI provides the graphical visualization of the regions where non-covalent interactions occur in real-space, differentiating hydrogen bonds, van der Waals interactions, and repulsive steric interactions [99]. The results for the interaction of I3C with chitosan and I3C with PEG are presented in Fig. 9c and d. The blue patches between the hydrogen atom of OH of I3C and the oxygen atom of chitosan or PEG are attributed to OH — O hydrogen bonds. As observed, in the case of I3C/chitosan, H-bond interaction is presented in two points, been more significant when compared with I3C/PEG system. Green patches appear in greater quantity for two systems that are associated with the Van der Walls interaction. These results showed that, beyond of the hydrogen bonds, the stabilization of the I3C molecule in the polymer matrix is stronger influenced by Van der Walls interactions. Besides this, is observed that I3C molecule presents a favorable interaction with both compounds (*i.e.* chitosan and PEG). This result is corroborated by release profile results (Fig. 7), where after 3 h the I3C-CS/PEG NP presents a less-release when compared with I3C-CS NP, proving the effect of the greatest interactions number among I3C, chitosan and PEG.

3.9. Cell viability evaluation

The evaluation of the antitumor activity of free and encapsulated I3C was carried out by the MTT assay in T24 human bladder carcinoma cell line after 24 h of exposure. This tumor cell has a representative nature of an invasive bladder tumor with a metastatic profile and therefore indicates an important parameter to assess the cytotoxic activity of these molecules [100]. Cell viability was given by the percentage of cells capable of maintaining mitochondrial activity after the time of exposure to cytotoxic agents.

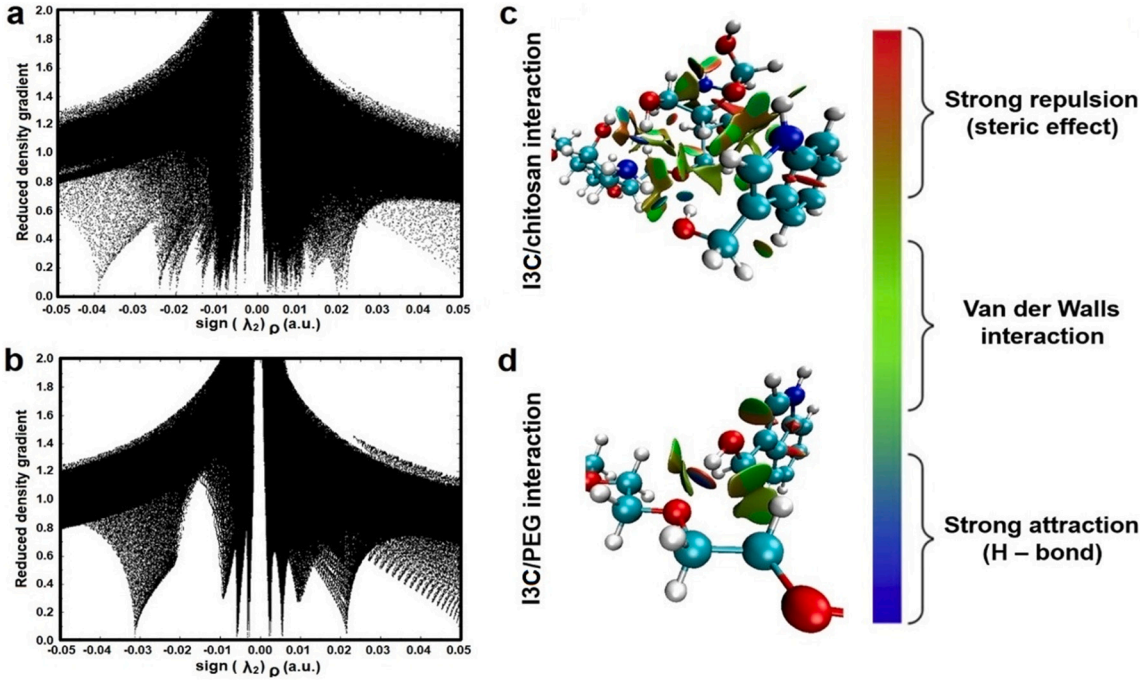

Fig. 9. NCI and RDG isosurfaces depicting non-covalent interaction (NCI) regions of (a,c) I3C/chitosan and (b,d) I3C/PEG interaction, respectively.

As far as we know, the evaluation of the cytotoxic effect of I3C on this cell line has not been presented in the literature to date. Thus, a large concentration range of free I3C (25 to 2000 μM) was evaluated in order to determine an optimal active spectrum and a dose response graph was plotted (Fig. 10a). Then, I3C-CS NP and I3C-CS/PEG NP were evaluated in a spectrum from 0.0 to 1000 μM (Fig. 10b). Furthermore, IC_{50} values were determined for each sample (Table 3).

The exposure of cells to 100 μM of free I3C showed a significant drop of 14% in cell viability ($p < 0.01$), followed by a reduction of 23% in a concentration of 250 μM ($p < 0.01$). When the cells were treated with 500 to 2000 μM, the viability of tumor cells decreased substantially, reaching a loss of mitochondrial activity of up to 87% for the highest concentration studied (2000 μM). In this way, it was possible to point that T24 human bladder carcinoma cells were sensitive to the action of free I3C from 100 μM. In addition, the IC_{50} for free HRP calculated was 344.7 μM.

As mentioned before, since there are no previous studies showing the use of I3C in T24 bladder cancer cells, the applicable comparisons to this work were given through the results obtained with other cell lines. In fact, several authors have demonstrated I3C cytotoxic activity for a wide variety of cell lines. Megna et al. (2016) evaluated the cell viability of different human colon cancer cells (DLD1, HCT116, HT-29, LS513, and RKO) after exposure to different concentrations of I3C (100, 500 and 1000 μM) for 24 h. As a result, none of the lineages studied showed cell viability reduction greater than 40% in the concentration of 500 μM [22]. Similarly, Choi et al. (2010) obtained a reduction of approximately 50% in cell viability of A549 lung carcinoma cells after 24 h of exposure to 500 μM of I3C [19]. Thus, the results obtained for the evaluation of free I3C cytotoxicity in human bladder carcinoma cells are satisfactory when compared with other studies presented in the literature and used as a basis for investigating the cytotoxic activity of I3C encapsulated on

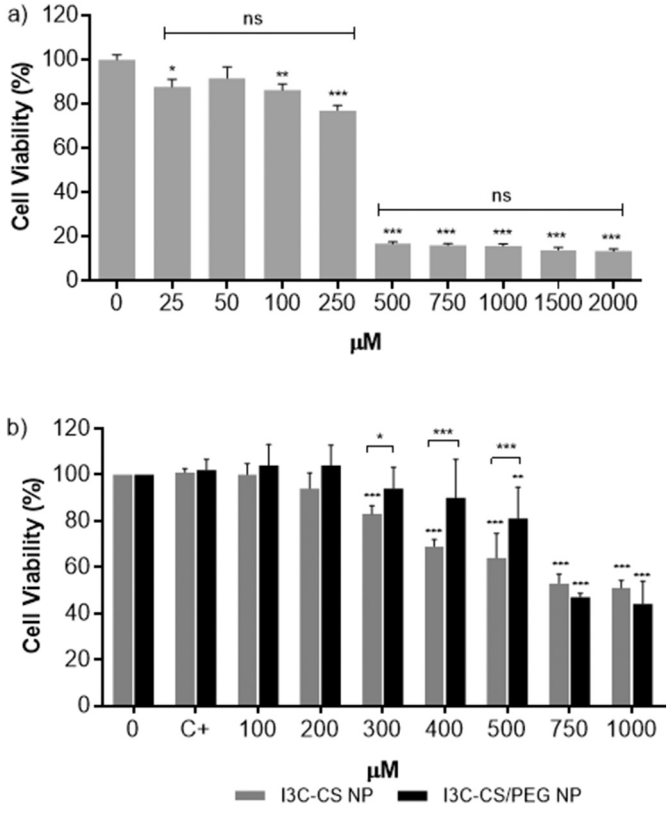

Fig. 10. Citotoxic effect of Free I3C (a), I3C-CS NP and I3C-CS/PEG NP (b) in different concentrations in T24 cell line for 24 h. C+ corresponds to the group that represents the pure nanoparticle. Data were analyzed by one-way ANOVA, followed by Tukey post-hoc. *** $p < 0.001$, ** $p < 0.01$ and * $p < 0.05$.

Table 3
IC_{50} values of cell viability from Free I3C, I3C-CS NP, and I3C-CS/PEG NP.

Sample	IC_{50} (μM)	SD
Free I3C	344.7	±11.2
I3C-CS NP	853.6	±23.0
I3C-CS/PEG NP	681.3	±11.4

NP CS and NP CS/PEG.

As seen in Fig. 10b, cellular response to the exposure of I3C-loaded nanoparticles is concentration-dependent. For the I3C-CS NP, a gradual decrease in cell viability was observed, reaching 83% at the concentration of 300 μM, 69% at 400 μM, and 64%, 53% and 51% at the concentrations of 500 μM, 750 μM, and 1000 μM, respectively ($p < 0.001$). On the other hand, a latency period to the cellular response to I3C-CS/PEG NP exposure was observed, with low cytotoxic activity (81% of viable cells) up to the concentration of 500 μM ($p < 0.01$). This can be justified by the increased release time of I3C for CS/PEG NP, as shown in the *in vitro* release study (Fig. 7). However, at higher concentrations, a considerable reduction in cell viability was observed, with a reduction of 47% and 44% at 750 μM and 1000 μM concentrations, respectively. There were no statistical significances between these values in comparison to the I3C-CS NP at the same concentrations.

Accordingly, the calculated IC_{50} for I3C-CS NP and I3C-CS/PEG NP were 853.6 ± 23.0 μM and 681.3 ± 11.4 μM, respectively, indicating that the presence of PEG results in a better cellular response to I3C (Table 3). The lower cytotoxic response, to the indole compound encapsulated in both nanoparticles in comparison to its free form (IC_{50} = 344.7 ± 11.2 μM), is based on the requirement of a higher time of cell exposure in order to ensure that the drug is completely released from nanoparticles and exert their cytotoxic activity.

Gehrcke et al. (2017), evaluated the cytotoxic activity of I3C encapsulated in rosehip oil nanocapsules in different concentrations (200, 300 and 500 μM) in breast cancer (MCF-7) and glioma (C6) using the sulforhodamine B (SRB) assay for 48 h. The authors obtained a cell death rate of up to 85% for both cell lines. The authors attribute the results to the ability of nanoparticles to increase the cellular internalization of the substance, resulting in the high cytotoxic activity of the compound [25]. This behavior may indicate an additional mechanism for cytotoxicity, added to the release profile of the molecule from nanoparticles at acid pH, such as that of cell culture and the tumor microenvironment. Thus, the tumor cells become exposed to agents released by nanoparticles in the external environment and undergo cytotoxic effects after internalization of the entire nanoparticles with the subsequent vesicular release of the agents.

I3C is a natural compound with recognized antitumor activity, and a well-defined chemical structure. However, it has some limitations related to factors that decrease serum level and bioavailability. The results obtained with cell viability for T24 human bladder carcinoma demonstrate a satisfactory susceptibility to I3C in concentrations greater than 500 μM after 24 h of exposure for both free and nanoencapsulated I3C. Our data indicate that polymeric nanoparticles based on chitosan and chitosan/PEG containing I3C can overcome the limitations contained in the I3C without changing the drug's anti-tumor characteristics, in addition to acting as a nanostructured system for the targeted delivery and/or controlled release of indole-3-carbinol and can be promise candidates to advanced investigations against bladder cancer.

4. Conclusion

In summary, chitosan and chitosan/PEG nanoparticles were successfully prepared to encapsulate I3C. The nanoparticles showed high and no statistical difference in encapsulation efficiency. Chitosan/PEG nanoparticles present a higher particle size than Chitosan nanoparticles before and after I3C encapsulation and all particles prepared present a positive surface charge. The encapsulation was evidenced by

physicochemical and thermal characterizations. Images of electron microscopy showed that spherical nanoparticles were formed successfully. Both nanoparticle formulations provided a burst initial release followed by a gradual and sustained release phase, but presented different kinetic profiles. Computational characterization reinforced the experimental results of release and was in accordance with physicochemical characterizations. The *in vitro* cytotoxicity study demonstrated that I3C-loaded nanoparticles, such as free I3C, have a considerable cytotoxic effect on T24 cell line in a dose-dependent manner. Thus, both I3C-loaded nanoparticles prepared in the present study could be potential candidates for bladder cancer therapy.

CRediT authorship contribution statement

Micael Nunes Melo: Conceptualization, Methodology, Validation, Formal analysis, Investigation, Data curation, Visualization, Writing - Original Draft.

Fernanda Menezes Pereira: Methodology and Investigation.

Matheus Alves Rocha: Methodology and Investigation.

Jesica Gonçalves Ribeiro: Methodology and Investigation.

Alexander Junges: Methodology and Investigation.

Wesley Formentin Monteiro: Investigation, Formal analysis, and Writing - Review & Editing.

Fernando Mendonça Diz: Methodology, Investigation, and Formal analysis, and Writing - Review & Editing.

Rosane Angélica Ligabue: Resources, and Writing - Review & Editing.

Fernanda Bueno Morrone: Resources, and Writing - Review & Editing.

Patrícia Severino: Resources, and Writing - Review & Editing.

Alini Tinoco Fricks: Supervision, Conceptualization, Resources, Project administration, Funding acquisition, Writing - Review & Editing.

Declaration of competing interest

The authors declare that they have no known competing financial interests or personal relationships that could have appeared to influence the work reported in this paper.

Acknowledgements

The Authors are grateful for the financial support from the Brazilian research funding agencies CAPES, CNPq and FAPITEC/SE.

References

[1] F. Bray, J. Ferlay, I. Soerjomataram, R.L. Siegel, L.A. Torre, A. Jemal, Global cancer statistics 2018: GLOBOCAN estimates of incidence and mortality worldwide for 36 cancers in 185 countries, CA Cancer J. Clin. 68 (2018) 394–424, https://doi.org/10.3322/caac.21492.

[2] T.J. Kim, K.S. Cho, K.C. Koo, Current status and future perspectives of immunotherapy for locally advanced or metastatic urothelial carcinoma: A comprehensive review, Cancers (Basel). 12 (2020). doi:https://doi.org/10.3390/cancers12010192.

[3] S.S. Chang, B.H. Bochner, R. Chou, R. Dreicer, A.M. Kamat, S.P. Lerner, Y. Lotan, J.J. Meeks, J.M. Michalski, T.M. Morgan, D.Z. Quale, J.E. Rosenberg, A. L. Zietman, J.M. Holzbeierlein, Treatment of non-metastatic muscle-invasive bladder cancer: AUA/ASCO/ASTRO/SUO guideline, J. Urol. 198 (2017) 552–559, https://doi.org/10.1016/j.juro.2017.04.086.

[4] O. Greco, L.K. Folkes, P. Wardman, G.M. Tozer, G.U. Dachs, Development of a novel enzyme/prodrug combination for gene therapy of cancer: horseradish peroxidase/indole-3-acetic acid, Cancer Gene Ther. 7 (2000) 1414–1420, https://doi.org/10.1038/sj.cgt.7700258.

[5] J. Koivunen, V. Aaltonen, S. Koskela, P. Lehenkar, M. Laato, J. Peltonen, Protein kinase C α/β inhibitor Go6976 promotes formation of cell junctions and inhibits invasion of urinary bladder carcinoma cells, Cancer Res. 64 (2004) 5693–5701, https://doi.org/10.1158/0008-5472.CAN-03-3511.

[6] J.A. Witjes, P.S. Kolli, Expert Opinion on Investigational Drugs Apaziquone for non-muscle invasive bladder cancer : a critical review Apaziquone for non-muscle invasive bladder cancer :, 3784 (2015). doi:https://doi.org/10.1517/13543784.17.7.1085.

[7] Y.M. Jeong, H. Li, S.Y. Kim, W.J. Park, H.Y. Yun, K.J. Baek, N.S. Kwon, J. H. Jeong, S.C. Myung, D.S. Kim, Photo-activated 5-hydroxyindole-3-acetic acid induces apoptosis of prostate and bladder cancer cells, J. Photochem. Photobiol. B Biol. 103 (2011) 50–56, https://doi.org/10.1016/j.jphotobiol.2011.01.011.

[8] V. Martel-frachet, M. Kadri, A. Boumendjel, X. Ronot, Bioorganic & Medicinal Chemistry Structural requirement of arylindolylpropenones as anti-bladder carcinoma cells agents 19 (2011) 6143–6148, https://doi.org/10.1016/j.bmc.2011.08.015.

[9] B. Prabhu, R. Padma, D. Alwin, N. Pazhanivel, D. Balakrishnan, S. Sundaresan, Journal of Experimental and Clinical Medicine Protective Effect of Diindolylmethane against N -Butyl- N - (4-hydroxybutyl) Nitrosamine-induced Bladder Carcinogenesis, J. Exp. Clin. Med. 6 (2014) 132–138. doi:https://doi.org/10.1016/j.jecm.2014.06.008.

[10] V.L. Maruthanila, J. Poornima, S. Mirunalini, Attenuation of carcinogenesis and the mechanism underlying by the influence of indole-3-carbinol and its metabolite 3,3′-diindolylmethane: a therapeutic marvel, Adv. Pharmacol. Sci. 2014 (2014), https://doi.org/10.1155/2014/832161.

[11] L.K. Folkes, P. Wardman, Oxidative activation of indole-3-acetic acids to cytotoxic species - a potential new role for plant auxins in cancer therapy, Biochem. Pharmacol. 61 (2001) 129–136, https://doi.org/10.1016/S0006-2952(00)00498-6.

[12] S. Safe, S. Papineni, S. Chintharlapalli, Cancer chemotherapy with indole-3-carbinol, bis(3′-indolyl) methane and synthetic analogs, Cancer Lett. 269 (2008) 326–338, https://doi.org/10.1016/j.canlet.2008.04.021.Cancer.

[13] J.R. Weng, C.H. Tsai, S.K. Kulp, C.S. Chen, Indole-3-carbinol as a chemopreventive and anti-cancer agent, Cancer Lett. 262 (2008) 153–163, https://doi.org/10.1016/j.canlet.2008.01.033.

[14] F. Fares, The Anti-Carcinogenic Effect of Indole-3-Carbinol and 3, 3'-Diindolylmethane and their Mechanism of Action, Med. Chem. (Los. Angeles). s1 (2014). doi:https://doi.org/10.4172/2161-0444.s1-002.

[15] R.K. Tiwari, L. Guo, H.L. Bradlow, N.T. Telang, M.P. Osborne, Selective responsiveness of human breast cancer cells to indole-3-carbinol, a chemopreventive agent, J. Natl. Cancer Inst. 86 (1994) 126–131, https://doi.org/10.1093/jnci/86.2.126.

[16] K.I. Jeon, J.K. Rih, H.J. Kim, Y.J. Lee, C.H. Cho, I.D. Goldberg, E.M. Rosen, I. Bae, Pretreatment of indole-3-carbinol augments TRAIL-induced apoptosis in a prostate cancer cell line, LNCaP, FEBS Lett. 544 (2003) 246–251, https://doi.org/10.1016/S0014-5793(03)00473-3.

[17] M. Qi, A.E. Anderson, D.Z. Chen, S. Sun, K.J. Auborn, Indole-3-carbinol prevents PTEN loss in cervical cancer in vivo, Mol. Med. 11 (2005) 59–63, https://doi.org/10.2119/2006-00007.Auborn.

[18] D.S. Kim, Y.M. Jeong, S.I. Moon, S.Y. Kim, S.B. Kwon, E.S. Park, S.W. Youn, K. C. Park, Indole-3-carbinol enhances ultraviolet B-induced apoptosis by sensitizing human melanoma cells, Cell. Mol. Life Sci. 63 (2006) 2661–2668, https://doi.org/10.1007/s00018-006-6306-1.

[19] H.S. Choi, M.C. Cho, H.G. Lee, D.Y. Yoon, Indole-3-carbinol induces apoptosis through p53 and activation of caspase-8 pathway in lung cancer A549 cells, Food Chem. Toxicol. 48 (2010) 883–890, https://doi.org/10.1016/j.fct.2009.12.028.

[20] G. Perez-Chacon, C. De Los Rios, J.M. Zapata, Indole-3-carbinol induces cMYC and IAP-family downmodulation and promotes apoptosis of Epstein-Barr virus (EBV)-positive but not of EBV-negative Burkitt's lymphoma cell lines, Pharmacol. Res. 89 (2014) 46–56, https://doi.org/10.1016/j.phrs.2014.08.005.

[21] X. Wang, H. He, Y. Lu, W. Ren, K. yu Teng, C. ling Chiang, Z. Yang, B. Yu, S. Hsu, S.T. Jacob, K. Ghoshal, L.J. Lee, Indole-3-carbinol inhibits tumorigenicity of hepatocellular carcinoma cells via suppression of microRNA-21 and upregulation of phosphatase and tensin homolog, Biochim. Biophys. Acta - Mol. Cell Res. 1853 (2015) 244–253. doi:https://doi.org/10.1016/j.bbamcr.2014.10.017.

[22] B.W. Megna, P.R. Carney, M. Nukaya, P. Geiger, G.D. Kennedy, Indole-3-carbinol induces tumor cell death: function follows form, J. Surg. Res. 204 (2016) 47–54, https://doi.org/10.1016/j.jss.2016.04.021.

[23] S.K. Murase, M. Aymat, A. Calvet, L.J. del Valle, J. Puiggalí, Electrosprayed poly (butylene succinate) microspheres loaded with indole derivatives: a system with anticancer activity, Eur. Polym. J. 71 (2015) 196–209, https://doi.org/10.1016/j.eurpolymj.2015.07.047.

[24] M. Gehrcke, M.H.M. Sari, L.M. Ferreira, A.V. Barbieri, L.M. Giuliani, V.C. Prado, J.M. Nadal, P.V. Farago, C.W. Nogueira, L. Cruz, Nanocapsules improve indole-3-carbinol photostability and prolong its antinociceptive action in acute pain animal models, Eur. J. Pharm. Sci. 111 (2018) 133–141, https://doi.org/10.1016/j.ejps.2017.09.050.

[25] M. Gehrcke, L.M. Giuliani, L.M. Ferreira, A.V. Barbieri, M.H.M. Sari, E.F. da Silveira, J.H. Azambuja, C.W. Nogueira, E. Braganhol, L. Cruz, Enhanced photostability, radical scavenging and antitumor activity of indole-3-carbinol-loaded rose hip oil nanocapsules, Mater. Sci. Eng. C. 74 (2017) 279–286, https://doi.org/10.1016/j.msec.2016.12.006.

[26] J.M. Song, A.R. Kirtane, P. Upadhyaya, X. Qian, S. Balbo, F. Teferi, J. Panyam, F. Kassie, Intranasal delivery of liposomal indole-3-carbinol improves its pulmonary bioavailability, Int. J. Pharm. 477 (2014) 96–101, https://doi.org/10.1016/j.ijpharm.2014.10.018.

[27] G. Yildiz, A. Yurt Kilcar, E.I. Medine, V. Tekin, O. Kozgus Guldu, F.Z. Biber Muftuler, PLGA encapsulation and radioiodination of indole-3-carbinol: investigation of anticancerogenic effects against MCF7, Caco2 and PC3 cells by in vitro assays, J. Radioanal. Nucl. Chem. 311 (2017) 1043–1052, https://doi.org/10.1007/s10967-016-4929-8.

[28] Q.-Y. Wei, Y.-M. Xu, A.T.Y. Lau, Recent Progress of Nanocarrier-Based Therapy for Solid Malignancies, Cancers (Basel). 12 (2020) 2783. doi:https://doi.org/10.3390/cancers12102783.

[29] A.C. Anselmo, S. Mitragotri, Nanoparticles in the clinic: An update, Bioeng. Transl. Med. 4 (2019). doi:https://doi.org/10.1002/btm2.10143.

[30] L. Bugnicourt, C. Ladavière, Interests of chitosan nanoparticles ionically cross-linked with tripolyphosphate for biomedical applications, Prog. Polym. Sci. 60 (2016) 1–17, https://doi.org/10.1016/j.progpolymsci.2016.06.002.

[31] L. Upadhyaya, J. Singh, V. Agarwal, A.C. Pandey, S.P. Verma, P. Das, R.P. Tewari, Efficient Water Soluble Nanostructured ZnO Grafted O-Carboxymethyl Chitosan/Curcumin-Nanocomposite for Cancer Therapy, Process Biochem, 2015, https://doi.org/10.1016/j.procbio.2014.12.029.

[32] L. Upadhyaya, J. Singh, V. Agarwal, R.P. Tewari, The implications of recent advances in carboxymethyl chitosan based targeted drug delivery and tissue engineering applications, J. Control. Release (2014), https://doi.org/10.1016/j.jconrel.2014.04.043.

[33] M. Abdel Mouez, N.M. Zaki, S. Mansour, A.S. Geneidi, Bioavailability enhancement of verapamil HCl via intranasal chitosan microspheres, Eur. J. Pharm. Sci. 51 (2014) 59–66, https://doi.org/10.1016/j.ejps.2013.08.029.

[34] J. Antoniou, F. Liu, H. Majeed, J. Qi, W. Yokoyama, F. Zhong, Physicochemical and morphological properties of size-controlled chitosan-tripolyphosphate nanoparticles, Colloids Surfaces A Physicochem. Eng. Asp. 465 (2015) 137–146, https://doi.org/10.1016/j.colsurfa.2014.10.040.

[35] T.A. Ahmed, B.M. Aljaeid, Preparation, characterization, and potential application of chitosan, chitosan derivatives, and chitosan metal nanoparticles in pharmaceutical drug delivery, Drug Des. Devel. Ther. 10 (2016) 483–507, https://doi.org/10.2147/DDDT.S99651.

[36] M.A. Mohammed, J.T.M. Syeda, K.M. Wasan, E.K. Wasan, An overview of chitosan nanoparticles and its application in non-parenteral drug delivery, Pharmaceutics. 9 (2017). doi:https://doi.org/10.3390/pharmaceutics9040053.

[37] J. Fang, H. Nakamura, H. Maeda, The EPR effect: unique features of tumor blood vessels for drug delivery, factors involved, and limitations and augmentation of the effect, Adv. Drug Deliv. Rev. 63 (2011) 136–151, https://doi.org/10.1016/j.addr.2010.04.009.

[38] F. Villanueva-Flores, A. Castro-Lugo, O.T. Ramírez, L.A. Palomares, Understanding cellular interactions with nanomaterials: Towards a rational design of medical nanodevices, Nanotechnology. 31 (2020). doi:https://doi.org/10.1088/1361-6528/ab5bc8.

[39] M.A. Ghaz-Jahanian, F. Abbaspour-Aghdam, N. Anarjan, A. Berenjian, H. Jafarizadeh-Malmiri, Application of chitosan-based nanocarriers in tumor-targeted drug delivery, Mol. Biotechnol. 57 (2015) 201–218, https://doi.org/10.1007/s12033-014-9816-3.

[40] R. Cheng, F. Meng, C. Deng, Z. Zhong, Bioresponsive polymeric nanotherapeutics for targeted cancer chemotherapy, Nano Today 10 (2015) 656–670, https://doi.org/10.1016/j.nantod.2015.09.005.

[41] L.E. Scheeren, D.R. Nogueira, L.B. Macedo, M.P. Vinardell, M. Mitjans, M. R. Infante, C.M.B. Rolim, PEGylated and poloxamer-modified chitosan nanoparticles incorporating a lysine-based surfactant for pH-triggered doxorubicin release, Colloids Surfaces B Biointerfaces. 138 (2016) 117–127, https://doi.org/10.1016/j.colsurfb.2015.11.049.

[42] A. Hefnawy, I.H. Khalil, K. Arafa, M. Emara, I.M. El-Sherbiny, Dual-ligand functionalized core-shell chitosan-based nanocarrier for hepatocellular carcinoma-targeted drug delivery, Int. J. Nanomedicine. Volume 15 (2020) 821–837, https://doi.org/10.2147/IJN.S240359.

[43] S. Caban-Toktas, A. Sahin, S. Lule, G. Esendagli, I. Vural, K. Karlı Oguz, F. Soylemezoglu, M. Mut, T. Dalkara, M. Khan, Y. Capan, Combination of paclitaxel and R-flurbiprofen loaded PLGA nanoparticles suppresses glioblastoma growth on systemic administration, Int. J. Pharm. 578 (2020) 119076, https://doi.org/10.1016/j.ijpharm.2020.119076.

[44] Y.-Q. Zhang, Y. Shen, M.-M. Liao, X. Mao, G.-J. Mi, C. You, Q.-Y. Guo, W.-J. Li, X.-Y. Wang, N. Lin, T.J. Webster, Galactosylated chitosan triptolide nanoparticles for overcoming hepatocellular carcinoma: enhanced therapeutic efficacy, low toxicity, and validated network regulatory mechanisms, nanomedicine nanotechnology, Biol. Med. 15 (2019) 86–97, https://doi.org/10.1016/j.nano.2018.09.002.

[45] E.J. Rupa, L. Arunkumar, Y. Han, J.P. Kang, J.C. Ahn, S. Jung, M. Kim, J.Y. Kim, D. Yang, G.J. Lee, Dendropanax Morbifera Estract-mediated ZnO nanoparticles loaded with Indole-3-Carbinol for enhancement of anticancer efficacy in the A549 human lung carcinoma cell line, Materials (Basel). 13 (2020) 1–16, https://doi.org/10.3390/ma13143197.

[46] P. Calvo, C. Remuñán-Lópes, J.L. Vila-Jato, M.J. Alonso, Novel hydrophilic chitosan – polyethylene oxide nanoparticles as protein carriers, J. Appl. Polym. Sci. 63 (1997) 125–132, https://doi.org/10.1002/(sici)1097-4628(19970103)63:1<125::aid-app13>3.0.co;2-410.1002/(sici)1097-4628(19970103)63:1<125::aid-app13>3.0.co;2-4.

[47] M.N. Melo, F.M. Pereira, M.A. Rocha, J.G. Ribeiro, F.M. Diz, W.F. Monteiro, R. A. Ligabue, P. Severino, A.T. Fricks, Immobilization and characterization of horseradish peroxidase into chitosan and chitosan / PEG nanoparticles: a comparative study, Process Biochem. 98 (2020) 160–171, https://doi.org/10.1016/j.procbio.2020.08.007.

[48] S.B. Aziz, A.S. Marf, E.M.A. Dannoun, M.A. Brza, R.M. Abdullah, The study of the degree of crystallinity, electrical equivalent circuit, and dielectric properties of polyvinyl alcohol (PVA)-based biopolymer electrolytes, Polymers (Basel). 12 (2020) 1–17, https://doi.org/10.3390/polym12102184.

[49] A. Allouche, Software news and updates Gabedit — a graphical user interface for computational chemistry softwares, J. Comput. Chem. 32 (2012) 174–182, https://doi.org/10.1002/jcc.

[50] T. Lu, F. Chen, Multiwfn: a multifunctional wavefunction analyzer, J. Comput. Chem. 33 (2012) 580–592, https://doi.org/10.1002/jcc.22885.

[51] W. Humphrey, A. Dalke, K. Schulter, VMD: visual molecular dynamics, J. Mol. Graph. 14 (1996) 33–38.

[52] H. Bahadar, F. Maqbool, K. Niaz, M. Abdollahi, Toxicity of nanoparticles and an overview of current experimental models, Iran. Biomed. J. 20 (2016) 1–11, https://doi.org/10.7508/ibj.2016.01.001.

[53] J.H. Jeong, J.-J. Kim, D.H. Bak, K.S. Yu, J.H. Lee, N.S. Lee, Y.G. Jeong, D.K. Kim, D.-K. Kim, S.-Y. Han, Protective Effects of Indole-3-Carbinol-Loaded Poly(lactic-co-glycolic acid) Nanoparticles Against Glutamate-Induced Neurotoxicity., J. Nanosci. Nanotechnol. 15 (2015) 7922–7928. doi:https://doi.org/10.1166/jnn.2015.11219.

[54] Y. Luo, T.T.Y. Wang, Z. Teng, P. Chen, J. Sun, Q. Wang, Encapsulation of indole-3-carbinol and 3,3′-diindolylmethane in zein/carboxymethyl chitosan nanoparticles with controlled release property and improved stability, Food Chem. 139 (2013) 224–230, https://doi.org/10.1016/j.foodchem.2013.01.113.

[55] K.V. Jardim, G.A. Joanitti, R.B. Azevedo, A.L. Parize, Physico-chemical characterization and cytotoxicity evaluation of curcumin loaded in chitosan/chondroitin sulfate nanoparticles, Mater. Sci. Eng. C. 56 (2015) 294–304, https://doi.org/10.1016/j.msec.2015.06.036.

[56] S. Bhattacharjee, DLS and zeta potential - what they are and what they are not? J. Control. Release 235 (2016) 337–351, https://doi.org/10.1016/j.jconrel.2016.06.017.

[57] C. He, Y. Hu, L. Yin, C. Tang, C. Yin, Effects of particle size and surface charge on cellular uptake and biodistribution of polymeric nanoparticles, Biomaterials. 31 (2010) 3657–3666, https://doi.org/10.1016/j.biomaterials.2010.01.065.

[58] B.S. Mahmoud, A.H. Alamri, C. McConville, Polymeric nanoparticles for the treatment of malignant gliomas, Cancers (Basel). 12 (2020) 1–28, https://doi.org/10.3390/cancers12010175.

[59] R. Ghasemi, M. Abdollahi, E.E. Zadeh, K. Khodabakhshi, mPEG-PLA and PLA-PEG-PLA nanoparticles as new carriers for delivery of recombinant human Growth Hormone (rhGH), Sci. Rep. (2018) 1–13, https://doi.org/10.1038/s41598-018-28092-8.

[60] A. Lucero-acu, C. Alejandra, RSC Advances Mathematical modeling and parametrical analysis of the temperature dependency of control drug release from biodegradable nanoparticles, (2019) 8728–8739. doi:https://doi.org/10.1039/c9ra00821g.

[61] G.R. Barbari, F.A. Dorkoosh, M. Amini, M. Sharifzadeh, F. Atyabi, S. Balalaie, N. R. Tehrani, M.R. Tehrani, A novel nanoemulsion-based method to produce ultrasmall , water-dispersible nanoparticles from chitosan , surface modified with cell-penetrating peptide for oral delivery of proteins and peptides, (2017) 3471–3483.

[62] A.V.A. Mariadoss, R. Vinayagam, V. Senthilkumar, M. Paulpandi, K. Murugan, B. Xu, K.M. Gothandam, V.S. Kotakadi, E. David, Phloretin loaded chitosan nanoparticles augments the pH-dependent mitochondrial-mediated intrinsic apoptosis in human oral cancer cells, Int. J. Biol. Macromol. 130 (2019) 997–1008, https://doi.org/10.1016/j.ijbiomac.2019.03.031.

[63] A. Valderrama N, C. Jacinto H, J. Lay, Y. Flores E, D. Zavaleta C, A.R. Delfín, Factorial design for preparing chitosan nanoparticles and its use for loading and controlled release of indole-3-acetic acid with effect on hydroponic lettuce crops, Biocatal. Agric. Biotechnol. 26 (2020) 101640. doi:https://doi.org/10.1016/j.bcab.2020.101640.

[64] J.J. Joseph, D. Sangeetha, T. Gomathi, Sunitinib loaded chitosan nanoparticles formulation and its evaluation, Int. J. Biol. Macromol. 82 (2016) 952–958, https://doi.org/10.1016/j.ijbiomac.2015.10.079.

[65] K.S.V. Krishna Rao, P. Ramasubba Reddy, Y.I. Lee, C. Kim, Synthesis and characterization of chitosan-PEG-Ag nanocomposites for antimicrobial application, Carbohydr. Polym. 87 (2012) 920–925, https://doi.org/10.1016/j.carbpol.2011.07.028.

[66] S.F. Hosseini, M.R. Soleimani, M. Nikkhah, Chitosan/sodium tripolyphosphate nanoparticles as efficient vehicles for antioxidant peptidic fraction from common kilka, Int. J. Biol. Macromol. 111 (2018) 730–737, https://doi.org/10.1016/j.ijbiomac.2018.01.023.

[67] Y. Wu, L. Li, S. Chen, J. Qin, X. Chen, D. Zhou, H. Wu, Synthesis, characterization, and crystallization behaviors of poly(D-lactic acid)-based triblock copolymer, Sci. Rep. 10 (2020) 1–12, https://doi.org/10.1038/s41598-020-60458-9.

[68] S. Anandhakumar, G. Krishnamoorthy, K.M. Ramkumar, A.M. Raichur, Preparation of collagen peptide functionalized chitosan nanoparticles by ionic gelation method: an effective carrier system for encapsulation and release of doxorubicin for cancer drug delivery, Mater. Sci. Eng. C. 70 (2017) 378–385, https://doi.org/10.1016/j.msec.2016.09.003.

[69] N.D. Suwarnakar, S.N. Nemade, P.V. Thorat, S.G. Gaikwad, Synthesis and characterization of sodium tripolyphosphate, J. Res. 03 (2017) 20–23, https://doi.org/10.1007/BF02704612.

[70] M. Anand, P. Sathyapriya, M. Maruthupandy, A.H. Beevi, Synthesis of chitosan nanoparticles by TPP and their potential mosquito larvicidal application, Front. Lab. Med. 2 (2018) 72–78, https://doi.org/10.1016/j.flm.2018.07.003.

[71] P. Kolhe, R.M. Kannan, Improvement in ductility of chitosan through blending and copolymerization with PEG: FTIR investigation of molecular interactions, Biomacromolecules. 4 (2003) 173–180, https://doi.org/10.1021/bm025689+.

[72] F. Li, S. Zhang, J. Liang, J. Wang, Effect of polyethylene glycol on the crystallization and impact properties of polylactide-based blends (2015), https://doi.org/10.1002/pat.3475.

[73] S. Maity, P. Mukhopadhyay, P.P. Kundu, A.S. Chakraborti, Alginate coated chitosan core-shell nanoparticles for efficient oral delivery of naringenin in diabetic animals—an in vitro and in vivo approach, Carbohydr. Polym. 170 (2017) 124–132, https://doi.org/10.1016/j.carbpol.2017.04.066.

[74] R. Balaji, S. Raghunathan, R. Revathy, Levofloxacin: formulation and in-vitro evaluation of alginate and chitosan nanospheres, Egypt. Pharm. J. 14 (2015) 30, https://doi.org/10.4103/1687-4315.154705.
[75] S. Shah, A. Pal, V.K. Kaushik, S. Devi, Preparation and characterization of venlafaxine hydrochloride-loaded chitosan nanoparticles and in vitro release of drug, J. Appl. Polym. Sci. 112 (2009) 2876–2887, https://doi.org/10.1002/app.29807.
[76] L.H. Gaabour, Spectroscopic and thermal analysis of polyacrylamide/chitosan (PAM/CS) blend loaded by gold nanoparticles, Results Phys. 7 (2017) 2153–2158, https://doi.org/10.1016/j.rinp.2017.06.027.
[77] M.A. Hassan, A.M. Omer, E. Abbas, W.M.A. Baset, T.M. Tamer, Preparation, physicochemical characterization and antimicrobial activities of novel two phenolic chitosan Schiff base derivatives, Sci. Rep. 8 (2018) 1–14, https://doi.org/10.1038/s41598-018-29650-w.
[78] T. Jayaramudu, G.M. Raghavendra, K. Varaprasad, G.V.S. Reddy, A.B. Reddy, K. Sudhakar, E.R. Sadiku, Preparation and characterization of poly(ethylene glycol) stabilized nano silver particles by a mechanochemical assisted ball mill process, J. Appl. Polym. Sci. 133 (2016) 1–8, https://doi.org/10.1002/app.43027.
[79] J.H. Yang, Y.S. Han, M. Park, T. Park, S.J. Hwang, J.H. Choy, New inorganic-based drug delivery system of indole-3-acetic acid-layered metal hydroxide nanohybrids with controlled release rate, Chem. Mater. 19 (2007) 2679–2685, https://doi.org/10.1021/cm070259h.
[80] G. Chitra, D.S. Franklin, S. Guhanathan, Indole-3-acetic acid based tunable hydrogels for antibacterial, antifungal and antioxidant applications, J. Macromol. Sci. Part A Pure Appl. Chem. 54 (2017) 151–163, https://doi.org/10.1080/10601325.2017.1265401.
[81] A. Bartyzel, A.A. Kaczor, H. Głuchowska, M. Pitucha, T.M. Wróbel, D. Matosiuk, Thermal and spectroscopic studies of 2,3,5-trisubstituted and 1,2,3,5-tetrasubstituted indoles as non-competitive antagonists of GluK1/GluK2 receptors, J. Therm. Anal. Calorim. 133 (2018) 935–944, https://doi.org/10.1007/s10973-018-7146-6.
[82] L. Alban, W.F. Monteiro, F.M. Diz, G.M. Miranda, C.M. Scheid, E.R. Zotti, F. B. Morrone, R. Ligabue, New quercetin-coated titanate nanotubes and their radiosensitization effect on human bladder cancer, Mater. Sci. Eng. C. 110 (2020) 110662, https://doi.org/10.1016/j.msec.2020.110662.
[83] I. Pilipenko, V. Korzhikov-Vlakh, V. Sharoyko, N. Zhang, M. Schäfer-Korting, E. Rühl, C. Zoschke, T. Tennikova, pH-sensitive chitosan–heparin nanoparticles for effective delivery of genetic drugs into epithelial cells, Pharmaceutics. 11 (2019). doi:https://doi.org/10.3390/pharmaceutics11070317.
[84] B.K. Patel, R.H. Parikh, P.S. Aboti, Development of oral sustained release rifampicin loaded chitosan nanoparticles by design of experiment, J. Drug Deliv. 2013 (2013) 1–10, https://doi.org/10.1155/2013/370938.
[85] R. Patel, B. Gajra, R. Parikh, G. Patel, Ganciclovir Loaded Chitosan Nanoparticles: Preparation and Characterization, J. Nanomed. Nanotechnol. 07 (2016). doi:https://doi.org/10.4172/2157-7439.1000411.
[86] G.S. Bangale, G. V Shinde, R. Ks, Formulation and Optimization of Nanoparticale by 3 2 Factorial Design for Colon Targeting, 7 (2019). doi:10.19080/GJPPS.2019.07.555702.
[87] Y. Ciro, J. Rojas, C.H. Salamanca, M.J. Alhajj, G.A. Carabali, Production and characterization of chitosan–polyanion nanoparticles by polyelectrolyte complexation assisted by high-intensity sonication for the modified release of methotrexate, Pharmaceuticals. 13 (2020). doi:https://doi.org/10.3390/ph13010011.
[88] A.M. Elwerfalli, A. Al-Kinani, R.G. Alany, A. Elshaer, Nano-engineering chitosan particles to sustain the release of promethazine from orodispersables, Carbohydr. Polym. 131 (2015) 447–461, https://doi.org/10.1016/j.carbpol.2015.05.064.
[89] T. Moodley, M. Singh, Polymeric mesoporous silica nanoparticles for enhanced delivery of 5-fluorouracil in vitro, Pharmaceutics. 11 (2019). doi:https://doi.org/10.3390/pharmaceutics11060288.
[90] E. Barim, F. Akman, Synthesis, characterization and spectroscopic investigation of N-(2-acetylbenzofuran-3-yl)acrylamide monomer: molecular structure, HOMO–LUMO study, TD-DFT and MEP analysis, J. Mol. Struct. 1195 (2019) 506–513, https://doi.org/10.1016/j.molstruc.2019.06.015.
[91] P. Demir, F. Akman, Molecular structure, spectroscopic characterization, HOMO and LUMO analysis of PU and PCL grafted onto PEMA-co-PHEMA with DFT quantum chemical calculations, J. Mol. Struct. 1134 (2017) 404–415, https://doi.org/10.1016/j.molstruc.2016.12.101.
[92] M.C. Özdemir, B. Özgün, E. Aktan, 1-Aryl-3,5-dimethylpyrazolium based tunable protic ionic liquids (TPILs), J. Mol. Struct. 1180 (2019) 564–572, https://doi.org/10.1016/j.molstruc.2018.12.027.
[93] H.F. Hizaddin, R. Anantharaj, M.A. Hashim, A quantum chemical study on the molecular interaction between pyrrole and ionic liquids, J. Mol. Liq. 194 (2014) 20–29, https://doi.org/10.1016/j.molliq.2013.12.041.
[94] M.A. Mumit, T.K. Pal, M.A. Alam, M.A.A.A.A. Islam, S. Paul, M.C. Sheikh, DFT studies on vibrational and electronic spectra, HOMO–LUMO, MEP, HOMA, NBO and molecular docking analysis of benzyl-3-N-(2,4,5-trimethoxyphenylmethylene)hydrazinecarbodithioate, J. Mol. Struct. 1220 (2020) 128715. doi:https://doi.org/10.1016/j.molstruc.2020.128715.
[95] R. Meenakshi, Spectral investigations, DFT based global reactivity descriptors, inhibition efficiency and analysis of 5-chloro-2-nitroanisole as π-spacer with donor-acceptor variations effect for DSSCs performance, J. Mol. Struct. 1127 (2017) 694–707, https://doi.org/10.1016/j.molstruc.2016.08.030.
[96] M. Karabacak, S. Bilgili, A. Atac, Molecular structure, spectroscopic characterization, HOMO and LUMO analysis of 3,3′-diaminobenzidine with DFT quantum chemical calculations, Spectrochim. Acta - Part A Mol. Biomol. Spectrosc. 150 (2015) 83–93, https://doi.org/10.1016/j.saa.2015.05.013.
[97] P. Bandyopadhyay, A. Karmakar, J. Deb, U. Sarkar, M.M. Seikh, Non-covalent interactions between epinephrine and nitroaromatic compounds: a DFT study, Spectrochim. Acta - Part A Mol. Biomol. Spectrosc. 228 (2020) 117827, https://doi.org/10.1016/j.saa.2019.117827.
[98] M. Bendjemai, H. Bouafia, B. Sahli, A. Dorbane, Uğur, G. Uğur, S. Mokrane, Insight into the role of weak interactions on optoelectronic properties of LiGaTe2-chalcopyrite under pressure effect: DFT-D3, NCI and QTAIM investigations, Phys. B Condens. Matter. 599 (2020) 412463. doi:https://doi.org/10.1016/j.physb.2020.412463.
[99] D. Imane, N. Leila, M. Fatiha, G. Abdelkrim, C. Mouna, L. Ismahan, B. Abdelazize, H. Brahim, Investigation of intermolecular interactions in inclusion complexes of pyroquilon with cucurbit[n]urils (n = 7,8) using DFT-D3 correction dispersion, J. Mol. Liq. 309 (2020). doi:https://doi.org/10.1016/j.molliq.2020.113233.
[100] Z.F. Zhao, K. Wang, F.F. Guo, H. Lu, Inhibition of T24 and RT4 human bladder cancer cell lines by heterocyclic molecules, Med. Sci. Monit. 23 (2017) 1156–1164. doi:10.12659/MSM.898265.